

Outdoor-to-Indoor 28 GHz Wireless Measurements in Manhattan: Path Loss, Environmental Effects, and 90% Coverage

Manav Kohli^{ID}, *Student Member, IEEE*, Abhishek Adhikari, Gulnur Avci, Sienna Brent, Aditya Dash, Jared Moser, Sabbir Hossain, *Student Member, IEEE*, Igor Kadota^{ID}, *Member, IEEE*, Carson Garland^{ID}, Shivan Mukherjee, *Student Member, IEEE*, Rodolfo Feick^{ID}, *Life Senior Member, IEEE*, Dmitry Chizhik^{ID}, *Fellow, IEEE*, Jinfeng Du^{ID}, *Member, IEEE*, Reinaldo A. Valenzuela^{ID}, *Life Fellow, IEEE*, and Gil Zussman^{ID}, *Fellow, IEEE*

Abstract— Outdoor-to-indoor signal propagation poses significant challenges to millimeter-wave link budgets. To gain insight into outdoor-to-indoor millimeter-wave at 28 GHz, we conducted an extensive measurement campaign consisting of over 2,200 link measurements in West Harlem, New York City, covering seven highly diverse buildings. A path loss model constructed over all measured links shows an average of 30 dB excess loss over free space at distances beyond 50 m. We find the type of glass to be the dominant factor in outdoor-to-indoor loss, with 20 dB observed difference between grouped scenarios with low- and high-loss glass. Other factors such as the presence of scaffolding, tree foliage, or elevated subway tracks, as well as difference in floor height are also found to have a 5–10 dB impact. We show that for urban buildings with high-loss glass, outdoor-to-indoor downlink capacity up to 400 Mb/s is supported for 90%

of indoor customer premises equipment by a base station up to 40 m away. For buildings with low-loss glass, such as our case study covering multiple classrooms of a public school, downlink capacity over 2.8/1.4 Gb/s is possible from a base station 57/133 m away within line-of-sight. We expect these results to help inform the planning of millimeter-wave networks targeting outdoor-to-indoor deployments in dense urban environments, as well as provide insight into the development of scheduling and beam management algorithms.

Index Terms— Millimeter-wave wireless, 28 GHz measurements, path loss models, wireless network planning, 5G-and-beyond networks.

I. INTRODUCTION

MILLIMETER-WAVE (mmWave) wireless is a key enabler of 5G-and-beyond networks. Its high-throughput potential makes it particularly viable for novel network solutions, such as fixed wireless access (FWA), to improve Internet connectivity helping to bridge the digital divide [2], [3]. A major challenge in using mmWave links, particularly in dense urban environments, is their high path loss, exacerbated in outdoor-to-indoor (O–I) scenarios. Therefore, measurement-based models of path loss under common environmental scenarios can support network planning for mmWave deployments, including those for providing indoor coverage. The development of algorithms (e.g., for beam management [4], [5], [6], link scheduling [7], [8], or transport layer enhancements [9], [10]) may also greatly benefit from such models and datasets.

While outdoor-to-outdoor (O–O) and indoor-to-indoor (I–I) propagation scenarios have been extensively measured [11], [12], [13], [14], [15], [16], [17], [18], [19], [20], [21], [22], [23], [24], [25], [26], [27], [28], [29], existing O–I datasets are relatively small in size [13], [14], [16], [30], [31], [32], [33]. Hence, in this paper we present the results of an extensive O–I mmWave measurement campaign that we conducted in a dense urban environment.

Measurements: As illustrated in Fig. 1, we conducted a large-scale measurement campaign in and around the COSMOS FCC Innovation Zone in West Harlem, New York City (NYC) [34], [35]. Using a 28 GHz channel sounder [18], we collected over 2,200 O–I measurements (comprising over

Manuscript received 25 December 2022; revised 3 October 2023; accepted 10 January 2024; approved by IEEE/ACM TRANSACTIONS ON NETWORKING Editor K. Chowdhury. Date of publication 26 January 2024; date of current version 18 June 2024. This work was supported in part by NSF under Grant CNS-1827923, Grant OAC-2029295, Grant EEC-2133516, Grant AST-2232455, Grant DGE-2036197, and Grant CNS-2148128; and in part by the Funds from Federal Agency and Industry Partners as specified in the NSF Resilient and Intelligent NextG Systems (RINGS) Program. The work of Rodolfo Feick was supported by the Chilean Research Agency Grant ANID PIA/APOYO under Grant AFB220004. Partial and preliminary version of this work appeared in Proc. ACM MobiHoc'22, Oct. 2022 [DOI: 10.1145/3492866.3549728]. (Corresponding author: Manav Kohli.)

Manav Kohli, Abhishek Adhikari, Gulnur Avci, Carson Garland, Shivan Mukherjee, and Gil Zussman are with the Department of Electrical Engineering, Columbia University, New York, NY 10027 USA (e-mail: mpk2138@columbia.edu).

Sienna Brent was with the Department of Electrical Engineering, Columbia University, New York, NY 10027 USA. She is now with AWS, New York, NY 10001 USA.

Aditya Dash was with the Department of Electrical Engineering, Columbia University, New York, NY 10027 USA. He is now with AMERGINT Technologies, Boulder, CO 80920 USA.

Jared Moser was with Stuyvesant High School, New York, NY 10282 USA. He is now with Department of Mechanical Engineering, Johns Hopkins University, Baltimore, MD 21218 USA.

Sabbir Hossain is with The City College of New York, New York, NY 10031 USA.

Igor Kadota was with the Department of Electrical Engineering, Columbia University, New York, NY 10027 USA. He is now with the Department of Electrical and Computer Engineering, Northwestern University, Evanston, IL 60208 USA.

Rodolfo Feick is with the Department of Electronics Engineering, Universidad Técnica Federico Santa María, Valparaíso 234000, Chile.

Dmitry Chizhik, Jinfeng Du, and Reinaldo A. Valenzuela are with Nokia Bell Labs, Murray Hill, NJ 07974 USA.

Digital Object Identifier 10.1109/TNET.2024.3355842

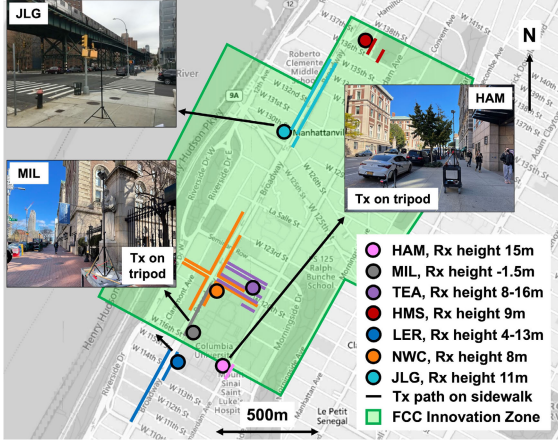


Fig. 1. Buildings and corresponding sidewalks where over 2,200 link measurements were collected in and around the COSMOS FCC Innovation Zone in West Harlem, NYC (more details are in Tables II and III, and Fig. 2).

32 million individual power measurements) across 44 O–I scenarios in seven very diverse buildings, covering a variety of construction materials and building utility. These 2,200 measurements correspond to 2,200 nominally line-of-sight (LOS) links, in which the outdoor transmitter emulating a base station (BS) is located on the same street as the building.

txtbfModels: We develop path gain models for each O–I scenario using a single-slope exponent and intercept fit to the measured data as a function of link distance, and record the cumulative distribution function (CDF) of the measured azimuth beamforming (BF) gain. We then group the O–I scenarios across several levels, gradually focusing on finer details which impact the models. Firstly, we consider all O–I scenarios as a single group, showing an average of 30 dB loss above free space at distances beyond 50 m. Secondly, we break down the O–I scenarios into groups on a per-building basis. Lastly, we group O–I scenarios to study specific effects, namely (i) the type of glass used for the windows (low- or high-loss glass), (ii) BS antenna placement in front of or behind an elevated subway track, (iii) customer premises equipment (CPE) placement on upper/lower floors of the building, (iv) the angle of incidence (AoI) of the mmWave signal into the building, (v) the presence of scaffolding outside of the window next to the CPE, and (vi) tree foliage on the street containing the BS. Using these groupings, we show, among other things: (i) little to no dependence on the particular nature of a building’s external construction, (ii) a 20 dB additional loss for the high-loss glass when compared to low-loss glass, (iii) a 10 dB difference in path gain for BSes blocked by elevated subway tracks or CPEs on different floors, and (iv) a 5–6 dB total impairment on link budget caused by scaffolding or tree foliage.

Case Study - Public School: We consider the Hamilton Grange public school in West Harlem as a detailed case study. The low path loss observed in this building along with its location in an area with below-average Internet access make it of particular interest for mmWave O–I coverage via FWA [3]. The path gain models associated with different classrooms are within 5 dB of each other across an 80 m span of BS placements. To aid further research into the viability of such FWA deployments, we shared the dataset for this case study via the NIST 5G Channel Model Alliance repository [36].

Coverage and Achievable Data Rates: We calculate achievable downlink capacity for up to 90% of indoor CPE locations one meter from the window using the path gain models for low-loss and high-loss glass. We also provide the corresponding extent of CPE–BS link distances for which these capacities may be achieved. We show that capacity in excess of 400 Mb/s is achievable in high-loss glass O–I scenarios for BS placements up to 40 m away. For low-loss glass O–I scenarios, capacity in excess of 2.8/1.4 Gb/s is achieved with the BS up to 57/133 m away, assuming a LOS path is available.

Angular Separation of Users: We evaluate this effect with two O–I scenarios in a classroom building using typical BS placements at the middle of a city block or the street corner. For indoor users located far from the BS, we find that inter-user-interference (IUI) can be significant, with a median correlation coefficient of 0.79 between directions of received power at the BS from other indoors users. IUI is reduced when the BS is located such that a wider range of angles is available.

Summary of Contributions: To the best of our knowledge, this paper presents the first extensive O–I mmWave measurement campaign with accompanying path gain models and 90% coverage metrics. It presents results from over 2,200 nominally LOS mmWave links, an order of magnitude more than prior studies. We anticipate that the results presented in this paper will serve two primary purposes: (i) generalizing path loss characteristics and corresponding downlink capacity at 28 GHz for indoors users across multiple building types, and (ii) presenting a set of broadly applicable effects to understand the impact they can introduce to the path loss and other propagation metrics in a dense urban environment. These impacts include up to a 20 dB increase in path loss depending on the type of window glass, and additional impacts caused by factors such as scaffolding or raised subway tracks. We hope this paper will shed light on the expected uncertainty in network planning for O–I mmWave deployments in dense urban environments as well as related network algorithm design. We also provide an extensive dataset from a unique case study at a public school building [36].

The rest of the paper is organized as follows. In Section II, we discuss related work. In Section III, we describe the measurement campaign, including equipment, locations, and method. In Section IV, we develop path gain models from the measurement data. In Section VII, we focus on the public school case study. In Section VIII we derive achievable data rates, and in Section IX we discuss the angular separation of indoors users in O–I scenarios. Finally, we conclude and discuss future work in Section X.

II. RELATED WORK

Table I provides an overview of a subset of prior efforts. As seen in the table, mmWave measurement studies typically require the use of specialized channel sounders and may be further categorized based on the type of measurement taken: O–O [12], [13], [17], [18], [19], [21], [22], [23], [24], [25], [26], [27], [29], I–I [11], [12], [13], [14], [16], [20], [21], [24], [28], [29], and O–I [13], [14], [16], [30], [32], [33], [37], as well as the frequency range and urban/suburban environment. Datasets that include outcomes of some of these

TABLE I
OVERVIEW OF PRIOR I-I, O-O, AND O-I MEASUREMENT STUDIES IN URBAN OR SUBURBAN ENVIRONMENTS USING VARIOUS FREQUENCY RANGES AND EQUIPMENT DESIGNS

Ref.	Type	Frequency	Environment	Tx Design	Rx Design	Bandwidth	# Links
[11]	I-I	28 GHz	Urban	Stationary Horn	Rotating Horn	Narrowband	>1,500
[12]	I-I, O-O	29 & 60 GHz	Urban & Suburban	Rotating Horn	Rotating Horn	200 MHz	785
[13]	I-I, O-O, O-I	28 GHz	Suburban	Stationary Horn	Stationary Horn	2 GHz	153
[14]	I-I, O-I	60 GHz	Urban	8x1 MIMO Array	8x2 MIMO Array	4 GHz	150
[16]	I-I, O-I	28 GHz	Urban	Gimbal-mounted Horn	Gimbal-mounted Horn	400 Mcps	18
[17]	O-O	60 GHz	Urban	36x8 Phased Array	36x8 Phased Array	2.16 GHz	15
[18]	O-O	28 GHz	Suburban	Stationary Horn	Rotating Horn	Narrowband	>2,000
[19]	O-O	28 GHz	Urban	Omnidirectional	Rotating Horn	Narrowband	>1,500
[30]	O-I	60 GHz	Urban	Stationary Horn	Stationary Horn	125 MHz	76
[31]	O-I	60 GHz	Suburban	Omnidirectional	Rotating Horn	Narrowband	160
[32]	O-I	28 GHz	Urban	8x2 Phased Array	8x2 Phased Array	400 MHz	29
[33]	O-I	28 GHz	Suburban	Stationary Slot Array	Stationary Parabolic Dish	50 MHz	43
<i>This work</i>	O-I	28 GHz	Urban	Omnidirectional	Rotating Horn	Narrowband	>2,200

TABLE II
MEASUREMENT LOCATIONS CONSIDERED, AS SHOWN IN FIGS. 1 AND 2. CORRESPONDING O-I SCENARIOS ARE IN TABLE III

Building Name	Abbreviation	Purpose	Year	Construction	Glass Type
Hamilton Hall	HAM	Classroom Building	1907	Brick & concrete	Low-e / High-loss
Miller Theatre	MIL	Theater	1918	Brick & concrete	Low-e / High-loss
Teachers' College	TEA	Classroom and Office Building	1924	Brick & concrete	Low-e / High-loss
M209 Hamilton Grange Middle School	HMS	Public School	1928	Brick & concrete	Traditional / Low-loss
Lerner Hall	LER	Student Center	1999	Brick & concrete	Low-e / High-loss
Northwest Corner Building	NWC	Laboratory Building	2008	Glass, metal, stone	Low-e / High-loss
Jerome L. Greene Science Center	JLG	Laboratory Building	2017	Glass & metal	Low-e / High-loss

studies are available in [29] and a review of several efforts at 60 GHz for a specific type of sounder is available in [24]. More generally, challenges and equipment demands for mmWave measurement are summarized in [38].

O-O measurements have focused on a variety of environments, including urban [13], [19], suburban [13], [18], and rural [39] mmWave deployment scenarios. Conversely, I-I measurements have primarily focused on one building type: offices [11], [14], [16], [28]. While such indoor environments represent a significant use case for mmWave wireless, especially with the recent approval of the 802.11ay standard [40], they represent only one building type.

Previous O-I measurements include those at a regional airport [13] and measurements of office space using a receiver (Rx) mounted on a robot and a stationary transmitter (Tx) [14]. Other forms of Tx/Rx mounting have been used, such as a Tx mounted on a van with indoors Rx [30]. Phased array antennas have also been used at the Tx and Rx [32], with 90° beamsteering capability and 5° resolution. Longer-term measurements have also been studied, including a four-day measurement with the indoor Rx and outdoor Tx both kept stationary [33]. Finally, 28 GHz O-I measurements have been collected at small-scale in NYC using a fixed Tx and Rx [16].

While some O-I measurements are available, to the best of our knowledge (and as can be seen in Table I), this paper is the *first large-scale, measurement-driven study of the O-I mmWave channel in a dense urban environment, leading to reliable statistical models for the path loss and beamforming gain degradation as well as quantitative insights for indoor propagation paths and realistic data rates*.

III. MEASUREMENT CAMPAIGN

In this section, we describe the measurement locations, equipment, and scenarios in the O-I measurement campaign.

Authorized licensed use limited to: Columbia University Libraries. Downloaded on June 03, 2025 at 19:42:51 UTC from IEEE Xplore. Restrictions apply.

A. Locations

Fig. 1 and Table II show seven buildings where measurements were conducted. These buildings are located in and around the FCC Innovation Zone [34] associated with the NSF PAWR COSMOS testbed [35] in West Harlem, NYC. In Fig. 1, the locations of these buildings are shown along with the corresponding outdoor sites (sidewalks, parking lot, and basketball court). Photos of these buildings are shown as insets in Fig. 1 and in Fig. 2. Table III lists the O-I scenarios for the seven buildings. Each building is described in detail below, including its location in upper Manhattan and the type of glass used, which is discussed in further detail in Section V-B.

HAM: *Hamilton Hall (1907).* HAM is a fifth-floor classroom at Hamilton Hall, located at the intersection of W 116th St. and Amsterdam Ave. This building has a brick-and-concrete construction shown in Fig. 2(a). The windows were replaced with modern, Low-e glass in recent years.

MIL: *Miller Theatre (1918).* MIL is the first-floor entrance to the Miller Theatre, located at the intersection of W 116th Street and Broadway. This brick-and-concrete building was renovated in 1988 with Low-e glass windows. The exterior construction is very similar to HAM, as seen in Fig. 2(b).

TEA: *Teachers' College (1924).* TEA covers a first-floor cafeteria and the first, second, and third floors of a library located within Russell Hall at Teachers' College, which has a complex facade constructed with brick and concrete seen in Fig. 2(c). The library and cafeteria overlook W 120th St. and W 121st St. between Broadway and Amsterdam Ave., respectively. The windows at TEA were renovated in 2001 with Low-e glass. The measurements at TEA were collected in Summer 2021, at a time when the library and cafeteria spaces were not actively used.

HMS: *Hamilton Grange Middle School (1960s).* HMS covers a set of third-floor classrooms at M209 Hamilton Grange

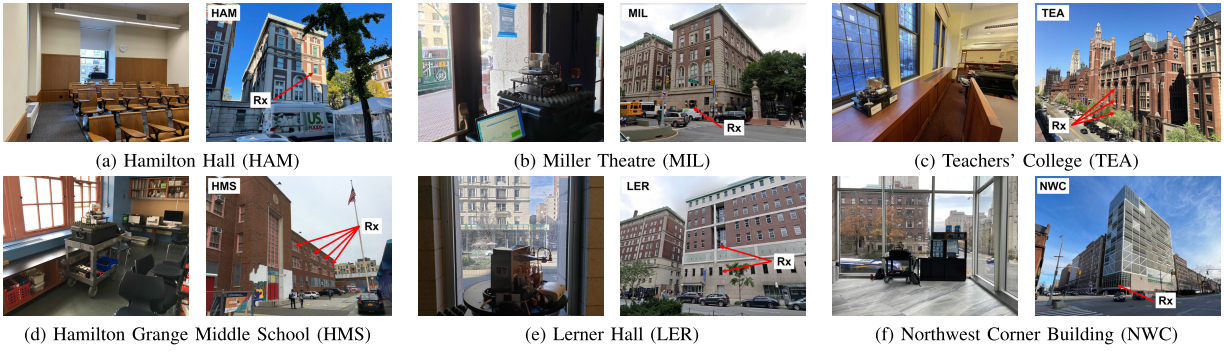


Fig. 2. Representative interior and exterior views of six of the seven locations (shown in Fig. 1 and Table II). Rx locations indicated on exterior views.

Middle School located in West Harlem, NYC, at Broadway and W 135th St. Each measured classroom contains a length of older single-glazed “traditional” windows spanning one-third of the exterior wall, shown in Fig. 2(d). Each classroom is an open space with no pillars, but has a relatively low ceiling due to the older building construction. The building is primarily constructed out of brick and concrete.

LER: Lerner Hall (1999). LER is a second- and fifth-floor student recreation space located at the intersection of W 115th St. and Broadway. The building exterior facing Broadway has a brick face. The windows on the fifth floor are recessed by two meters into the building face, as seen in Fig. 2(e). They are glazed with Low-e glass.

NWC: Northwest Corner Building (2008). NWC is a coffee shop within the second floor of the Northwest Corner Building at the intersection of W 120th St. and Broadway. The building exterior is primarily made of glass and metal. The coffee shop is an open space with floor-to-ceiling Low-e glass windows overlooking the intersection seen in Fig. 2(f). Walls encircle the rest of the coffee shop not facing the streets. Measurements were taken at NWC in Fall 2020, Summer 2021, and Fall 2021. In 2020, the coffee shop did not permit patrons to sit due to COVID-19 social distancing requirements.

JLG: Jerome L. Greene Science Center (2017). JLG is a third-floor corner office and common area at the Jerome L. Greene Science Center, located on the northwest corner of W 129th St. and Broadway. The exterior construction is primarily made of glass and metal. In particular, the common area and corner office are encircled by floor-to-ceiling Low-e glass overlooking Broadway, including the only elevated portion of the 1 line of the NYC Subway, visible in the top-left inset in Fig. 1.

B. Equipment

We utilize a 28 GHz channel sounder consisting of a separate Tx and Rx, which is described in detail in [18] and [19]. The Tx can be seen in the inset photographs within Fig. 1 and the Rx is shown in the various indoor photographs in Fig. 2; both can be seen together in Fig. 3(a). The Tx is equipped with an omnidirectional antenna with 0 dBi gain, and transmits a +22 dBm continuous-wave tone. The Rx, mounted on a rotating platform, is fed by a 24 dBi horn antenna (14.5 dBi in azimuth) with 10° half-power beamwidth in both azimuth and elevation. The radiation patterns of both the Tx and Rx antennas were comprehensively measured in an anechoic chamber so that the precise, non-idealized antenna pattern is

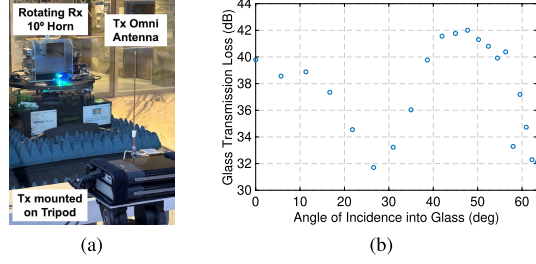


Fig. 3. Measurement to study impact of AoI on path loss. (a) Equipment setup and (b) measured glass transmission loss as a function of AoI.

used when calculating the results in Section IV [18]. The antenna feeds a mixer which downconverts the received signal to 100 MHz intermediate frequency (IF). The IF signal is then passed through two switchable-gain amplifiers and a 20 kHz-wide bandpass filter. Finally, the IF signal’s power is recorded by a power meter sampling at 740 samples per second. The power meter samples are collected on a platform-mounted microcontroller, which also keeps track of angular direction.

C. Scenarios

For the scenarios in Table III, we placed the rotating Rx indoors (emulating a CPE) and the omnidirectional Tx outdoors (emulating a BS). The Tx was moved along a linear path, such as a sidewalk, at a height of 3.4 m. This emulates lightpole deployments of mmWave BSes along streets, which are slated for widespread use in NYC and other urban areas [41], [42]. A total of 44 scenarios are listed in Tables III and IV. For the measurements in Table III, an O-I scenario is defined by the indoor Rx placement within a given building and the outdoors Tx path. In each scenario, we placed the Tx at set intervals along the path whose length is defined by the “Range” column in Table III. At each such location (namely, every interval), we measured a link to the indoor Rx. The number of links for each scenario is listed in Table III. For each link measurement, the rotating Rx measured the channel for 20 seconds, corresponding to 40 full rotations at 120 RPM. A power reading was taken 740 times per second, providing at least 14,800 power readings per link measurement.

Using the same equipment but in different setups, four additional O-I scenarios were studied, which are listed in Table IV. The first and second, detailed in Section VII-B, investigate the path loss and signal propagation within an interior hallway at HMS. The Tx was kept stationary outdoors and the Rx moved indoors. The third and fourth, detailed in Section IX,

TABLE III

40 O-I MEASUREMENT SCENARIOS WITH COMPUTED SLOPE-AND-INTERCEPT PATH GAIN MODELS AND MEDIAN AZIMUTH BEAMFORMING GAIN $G_{az,m}$. NO MODEL IS PROVIDED FOR JLG-E-E, DUE TO THE LIMITED RANGE OF TX-RX LINK DISTANCES COVERED

Name	Color	Group	Tx Path (m)	Step (m)	# Links	Slope (dB)	Intercept (dB)	RMS (dB)	$G_{az,m}$ (dB)
HAM-S-E	Pink	HAM	61	1	62	-6.61	-23.7	3.5	11.1
MIL-N-E	Gray	MIL	155	2.5	76	-3.53	-59.1	2.8	11.0
TEA-S-N-1-Sc	Purple	TEA	230	6/8	35	-2.56	-95.3	5.6	11.0
TEA-S-S-1-Sc	Purple	TEA	228	4/8	45	-3.49	-75.1	4.8	10.9
TEA-S-S-2	Purple	TEA	155	3	52	-5.52	-40.5	2.6	7.7
TEA-S-S-3	Purple	TEA	232	3	77	-5.13	-36.1	3.3	8.8
TEA-S-Bal-1	Purple	TEA	85	3	29	-1.61	-107.9	4.7	9.7
TEA-S-Bal-2	Purple	TEA	85	3	29	-0.69	-111.3	4.2	7.8
TEA-S-Bal-3	Purple	TEA	37	3	13	-5.20	-33.6	4.3	10.0
TEA-N-N	Purple	TEA	243	3	68	-4.45	-53.0	4.1	10.8
TEA-N-S	Purple	TEA	243	3	81	-4.80	-41.0	4.1	10.1
HMS-Lot-307	Maroon	HMS	62	1	63	-3.22	-60.4	1.6	10.4
HMS-Lot-317	Maroon	HMS	62	1	63	-3.48	-52.0	3.4	11.5
HMS-Lot-321	Maroon	HMS	62	1	63	-4.12	-44.1	3.4	11.8
HMS-Lot-323	Maroon	HMS	62	1	63	-4.10	-47.2	2.5	9.9
HMS-Lot-325	Maroon	HMS	62	3	22	-3.40	-54.8	2.5	10.8
HMS-Court-307	Maroon	HMS	42	1	43	-5.47	-3.9	2.9	13.3
HMS-Court-317	Maroon	HMS	39	1	40	-6.48	11.2	3.2	12.0
HMS-Court-321	Maroon	HMS	57	1	58	-8.50	51.1	3.1	11.0
HMS-Court-323	Maroon	HMS	57	1	58	-8.13	43.6	1.6	9.8
HMS-Court-325	Maroon	HMS	58	1	59	-1.88	-84.3	2.2	10.2
LER-S-W-5	Blue	LER	298	3	96	-5.29	-19.6	3.0	10.8
LER-S-W-2	Blue	LER	110	8	14	-6.72	-22.8	4.2	9.4
LER-S-E-2	Blue	LER	95	6	23	-3.97	-75.2	3.8	9.4
NWC-N-W-Sc-NLe	Orange	NWC	227	3/6	70	-3.26	-76.0	3.5	11.1
NWC-N-W-NSc-NLe	Orange	NWC	197	3/6	65	-3.03	-76.9	4.7	12.8
NWC-N-E-NSc-Le	Orange	NWC	201	3	60	-3.52	-73.0	1.9	11.2
NWC-N-E-NSc-NLe	Orange	NWC	174	3	51	-3.38	-71.5	2.5	12.1
NWC-E-N-Sc-NLe	Orange	NWC	131	3	44	-4.62	-56.4	2.0	8.8
NWC-E-N-NSc-NLe	Orange	NWC	131	3	44	-4.83	-48.7	2.9	11.1
NWC-E-S-NSc-Le	Orange	NWC	242	3	78	-3.08	-83.2	2.8	10.8
NWC-S-E-NSc-NLe	Orange	NWC	105	1	106	-3.30	-86.7	4.9	9.8
NWC-S-W-NSc-NLe	Orange	NWC	180	2/3/6	72	-3.36	-74.9	4.5	10.9
NWC-W-S-NSc-Le	Orange	NWC	153	3	46	-4.36	-55.4	4.2	12.1
NWC-W-S-NSc-NLe	Orange	NWC	135	3	40	-4.85	-42.3	3.2	13.7
NWC-W-N-NSc-Le	Orange	NWC	146	3	47	-2.70	-92.2	2.2	8.3
NWC-W-N-NSc-NLe	Orange	NWC	173	3	56	-2.02	-102.4	3.2	10.3
JLG-N-W	Cyan	JLG	291	3/6	75	-2.94	-72.5	2.5	10.8
JLG-N-E	Cyan	JLG	224	3	68	-3.20	-77.7	2.3	8.9
JLG-E-E	Cyan	JLG	49	3	17	N/A	N/A	N/A	N/A

TABLE IV

FOUR ADDITIONAL O-I MEASUREMENT SCENARIOS WITH DIFFERENT TX AND RX LOCATIONS

Name	Group	Range (m)	# Links	Tx & Rx placement	Purpose
HMS-Lot-Hallway	HMS	57	58	Tx fixed outdoors, Rx moved inside	Characterizing deep indoor spaces (§VII-B)
HMS-Court-Hallway	HMS	57	58	Tx fixed outdoors, Rx moved inside	Characterizing deep indoor spaces (§VII-B)
TEA-S-Corner-1-Reverse	TEA	230	17	Rx fixed outdoors, Tx moved inside	Angular separation of indoor users (§IX)
TEA-S-Middle-1-Reverse	TEA	111	19	Rx fixed outdoors, Tx moved inside	Angular separation of indoor users (§IX)

investigate the angular separation between different indoors users, which is a consideration for their simultaneous support by the outdoors BS. The Rx was kept stationary outdoors and the Tx moved indoors. *In total, we took over 2,200 Tx-Rx link measurements representing over 32 million individual power measurements.*

IV. MEASUREMENT RESULTS AND ANALYSIS

In this section, we use the data obtained from the measurement campaign to develop path gain models for the 40 O-I scenarios covered in Fig. 1 and Table III. We then describe our approach to analyzing the data in this and subsequent sections. Each scenario name in Table III is structured as **LOC-X-Y-#**, where **LOC** is a location in Fig. 1, **X** is the cardinal direction of the Tx relative to the Rx, **Y** is the

sidewalk along which the Tx was moved, and **#** is the floor of the building in which the Rx was placed, if applicable. In some O-I scenarios at **TEA**, the Tx was moved along an outdoors balcony on the opposite side of the street instead, indicated by “Bal”. The measurements at **HMS** use a different naming scheme. The first value refers to the Tx path that was used (along a parking lot or basketball court) and the number refers to the classroom where the Rx was. Lastly, the measurements for **NWC** have additional descriptors which mark if the measurement has (no) scaffold ((N)Sc) or (no) tree leaves ((N)Le). Two measurements from **TEA** are also marked with the scaffolding descriptor.

Table III shows the range of parameter values for the O-I scenarios studied, which have large differences even for scenarios at the same building. For example the measure-

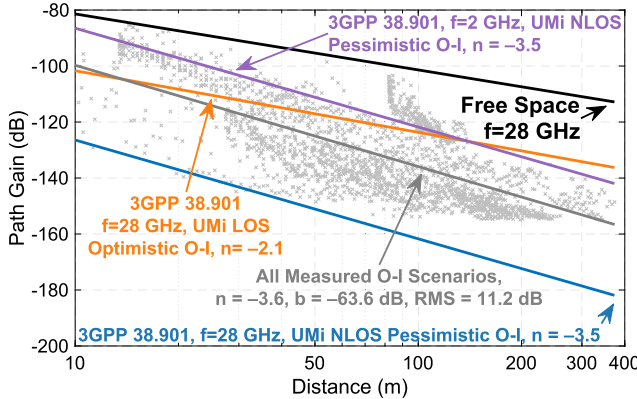


Fig. 4. Comparison of the path gain model for the grouping of all O-I scenarios to optimistic and pessimistic models developed from 3GPP UMi path loss predictions for different types of glass.

ments **HMS-Court-321** and **HMS-Court-325**, where the only difference is the classroom in which the Rx was located. We can develop better insight by grouping O-I scenarios in certain ways. In Section IV-B, we fit a single model across all O-I scenarios, and compare this large ensemble of data to 3GPP predictive models [43]. We show that the majority of measured Tx-Rx links fall between optimistic and pessimistic O-I predictive models. Next, in Section V-A, we group the O-I scenarios by the building containing the Rx, computing a path gain model for each, along with distributions of the azimuth beamforming gain and temporal k -factor. Significant differences are found between buildings with outwardly similar appearances.

In Section V-B, we group O-I scenarios based on the type of window glass used, considering “traditional” and modern Low-e glass, as measured in Fig. 3(b). In Section VI-A, we consider the impact from various BS and CPE placements, including the BS behind/in front of an elevated subway track, the CPE on different floors of the same building, and AoI less or greater than 45° into the window nearest to the CPE. Lastly, Section VI-B presents an analysis on the impact of scaffolding surrounding the building containing the CPE and leaves on trees lining the sidewalk containing the BS.

A. Measurable Parameters

Four parameters are calculated from the data for each measured Tx-Rx link: (i) path gain, $G_{\text{path}}(d)$ as a function of Tx-Rx link distance d , (ii) azimuth angular spectra of the received power $\bar{S}(d, \phi)$, (iii) effective azimuth beamforming gain $G_{\text{az}}(d)$, representing the effect of angular spread, and (iv) temporal Rician k -factor $K(d)$, defined as the ratio of steady to time-varying channel power.

To compute $G_{\text{path}}(d)$, we note that averaging the received power $P_{\text{horn}}(d, \phi)$ over all directions ϕ gives the equivalent power that would be received by an omnidirectional antenna [18]:

$$P_{\text{omni}}(d) = \frac{1}{2\pi} \int_0^{2\pi} P_{\text{horn}}(d, \phi) d\phi. \quad (1)$$

$P_{\text{horn}}(d, \phi)$ is the sole quantity measured by the channel sounder. By taking the average $\bar{P}_{\text{omni}}(d)$ over all turns, we can

compute the path gain $G_{\text{path}}(d)$ as

$$G_{\text{path}}(d) = \frac{\bar{P}_{\text{omni}}(d)}{(P_{\text{Tx}} \cdot G_{\text{el}})}, \quad (2)$$

where P_{Tx} is the transmit power, and $G_{\text{el}}(d)$ is the elevation gain, calculated from the antenna patterns of the Tx and Rx measured in an anechoic chamber. $G_{\text{el}}(d)$ is used to correct for the misalignment of the Rx horn as it spins in azimuth.

The power angular spectra is computed by averaging $P_{\text{horn}}(d, \phi)$ across all complete turns the Rx makes during one measurement:

$$\bar{S}(d, \phi) = \frac{1}{N} \sum_{i=1}^N P_{\text{horn}}^{(i)}(d, \phi), \quad (3)$$

where $P_{\text{horn}}^{(i)}(d, \phi)$ represents the power recorded at angle ϕ on the i^{th} turn. $\bar{S}(d, \phi)$ can then be directly used to compute $G_{\text{az}}(d)$ as

$$G_{\text{az}}(d) = \frac{\max_{\phi} \{\bar{S}(d, \phi)\}}{\bar{P}_{\text{omni}}(d)}. \quad (4)$$

$G_{\text{path}}(d)$ and $G_{\text{az}}(d)$ are important parameters as they will define the signal-to-noise ratio (SNR) of a Tx-Rx link; we use the SNR to study the achievable data rates in Section VIII. The model parameters describing $G_{\text{path}}(d)$ and the median value of $G_{\text{az}}(d)$, $G_{\text{az,m}}$, are given for each O-I scenario in Table III. Any $G_{\text{az}}(d)$ below the nominal value of 14.5 dB indicates beamforming gain degradation resulting from environmental scattering. We use $\bar{S}(d, \phi)$ to understand O-I propagation paths in Section VII-B and the angular separation of different indoors users in Section IX.

Lastly, $K(d)$ represents the level of time variation in the wireless channel, and is computed using the method of moments [44]. $K(d)$ represents the ratio of the steady to variable channel power, and thus a measured $K(d)$ of 20 dB indicates a steady power that is 100× stronger than time-varying power.

B. Comparison to 3GPP Predictive Models

We first aggregate all O-I scenarios in Table III into a single group, and compute the path gain model as described in Section IV-A. Fig. 4 shows this path loss model, along with pessimistic and optimistic models developed from 3GPP TR 38.901 [43]. The model for the group of all O-I scenarios shows an excess loss above free space of at least 30 dB beyond 50 m link distance. The pessimistic model is defined as $PL_{\text{pess}}(d) = PL_{\text{O-O,NLOS}}(d) + PL_{\text{O-I,High}}$, which is the sum of the non-line-of-sight (NLOS) urban street canyon model (USCM) and building transmission loss with Low-e glass. We use the NLOS model for two reasons. Firstly, beyond 52 m, the 3GPP NLOS probability will exceed 50% [43]; the majority of our measurement data is at distances larger than 52 m and thus prone to occlusion by trees and other sidewalk clutter. Secondly, this model provides an upper bound for the expected path loss. Similarly, to give a lower bound on the expected path loss, the optimistic model is defined as $PL_{\text{opt}}(d) = PL_{\text{O-O,LOS}}(d) + PL_{\text{O-I,Low}}$, using the LOS USCM and building transmission loss with “traditional” multi-pane

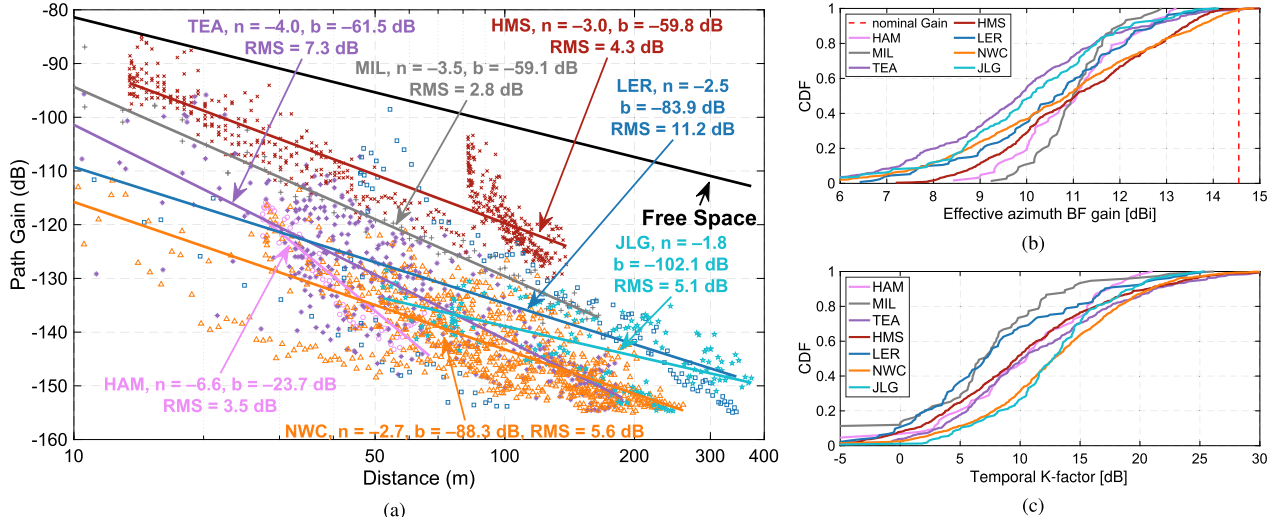


Fig. 5. Measurement results grouped by building: (a) average path gain as a function of the 3-dimensional Tx-Rx link distance, with models for each building plotted and noted, (b) CDF of azimuth beamforming gain, (c) CDF of temporal k -factor.

glass. In addition, a pessimistic model at 2 GHz is included in the figure. In all 3GPP predictive models, the BS height is 10 m and the CPE height is 3.5 m, reflecting the typical height of the Rx and Tx in our measurements, respectively.

The 40 O-I scenario measurements predominantly fall between the two 28 GHz models. There are a number of points which lie above the optimistic line; these are mostly from **HMS**. This is largely due to the single-pane “traditional” glass windows, which should produce lower path loss compared to the predicted $PL_{O,I,\text{Low}}$. The tendency for the measured path gain to be either in between pessimistic and optimistic models, or greater than an optimistic one, was previously observed in O-O measurements [19] employing a similar measurement methodology and equipment. The slope of the measured O-I model is $n = -3.7$, which is similar to the pessimistic 2 GHz and 28 GHz models, suggesting that the outdoor paths align more closely with the NLOS USCM. Lastly, we observe that the measured Tx-Rx links lie an average of 16 dB below the 2 GHz pessimistic model, with some points as far as 40 dB below. This highlights the challenge of O-I propagation at higher frequencies as outlined in Section I.

V. THE IMPACT OF BUILDING CONSTRUCTION

The measured buildings described in Section III-A cover a large range of construction materials and architectural designs, allowing the evaluation of path loss models in relation to these factors. In this section, we first calculate the path loss models for O-I scenarios grouped by building, and then evaluate the effect of the type of window glass used.

A. Different Buildings

Fig. 5 shows the measured path gain with best-fit models, azimuth beamforming gain, and temporal k -factor for all building groups. Most notably, Fig. 5(a) shows that **HMS** experiences path gain 10–25 dB higher than other buildings at 50 m three-dimensional Euclidean distance between Tx and Rx; this effect is evaluated in further detail in Section V-B. Fig. 5(b) shows that the median azimuth beamforming gains for all buildings are within 1.2 dB of each other, degraded

by 3.3–4.5 dB from the nominal gain of the Rx antenna. We attribute this gain degradation to the scattering effect of the complex urban environment, allowing the mmWave signal to impinge on the Rx from directions other than a direct shot. We also note that buildings with larger windows (**TEA**, **NWC**, and **JLG**) tend to have lower azimuth beamforming gain than others. This is likely due to the larger windows permitting signal penetration from a wider range of directions for a given Tx location on the sidewalk.

Fig. 5(c) shows that the median temporal k -factor can vary by around 8 dB. We expect that this effect is predominantly from the time-varying outdoor environment, as the indoor environment was considerably more stable. **JLG** and **NWC** have a higher temporal k -factor than other locations. This may be due to several reasons, including the larger windows permitting higher “visibility” into the outdoor time-varying environment, as well as the characteristics of the outdoor environment itself. We note that **JLG** and **NWC** are each located on corners of Broadway, a comparatively busy street with upwards of 1,000 vehicles passing per hour during the day [45]. On the other hand, **TEA**, which experiences a lower temporal k -factor, is located on the perpendicular 120th St., which experiences only around 500 vehicles per hour [45].

The large differences in Fig. 5(a) between buildings of similar construction (for example, **HAM** and **MIL** as shown in Fig. 2) suggest that building construction alone is not a good indicator of the expected loss.

B. Modern (Low- e) and Traditional Glass

In order to understand the specific factors that may impact the path loss for a building, we first group the measurements based on the type of glass. “Traditional” glass, often used in buildings predating the widespread availability of float glass in the 1960s, typically has less than 1 dB loss at 28 GHz [46]. Modern Low- e glass can have losses in excess of 25 dB [47]; Fig. 3(b) shows a measured normal incidence loss of 40 dB from Low- e glass at **NWC**, similar to that observed in other O-I measurement campaigns [37]. Loss as high as 50 dB through concrete walls at 28 GHz [48] implies that the majority

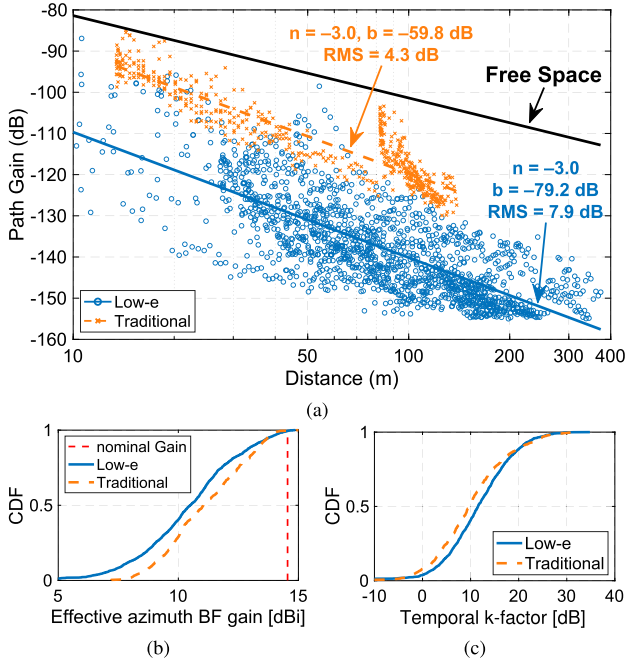


Fig. 6. Results for O-I scenarios grouped by their use of “traditional” or Low-e glass. (a) Path gain models for each type of glass, and CDFs of (b) effective azimuth beamforming gain and (c) temporal k -factor.

of the mmWave signal will be received via windows, suggesting them to be a significant factor impacting path loss.

HMS uses traditional glass, while the other six locations use Low-e glass; the windows at older buildings have been replaced in recent years. The results of this analysis are presented in Fig. 6, with the path gain models for both categories in Fig. 6(a). The models have identical slopes, with the difference being a uniform 20 dB additional loss experienced by the buildings with Low-e glass. This significant difference suggests a need to consider the building glass type during the RF planning stage of mmWave network deployment.

The results for the azimuth beamforming gain and temporal k -factor are shown in Figs. 6(b) and 6(c). These two quantities are very similar, with an azimuth beamforming gain degradation of 3.5–4.5 dB and median k -factor value of 10–12 dB. This is to be expected, as these values are influenced primarily by the overall measurement environment rather than by the type of glass. The results indicate a moderate level of beamforming gain degradation and reasonable channel stability over time; the median temporal k -factor is 10 dB, indicating that the time-varying component of the received signal is one-tenth of the total power.

VI. LOCATIONAL AND ENVIRONMENTAL EFFECTS

Having scaled down the analytical scope from all scenarios in a single model (Section IV-B), to separation by building and the specific type of glass (Section V), we now consider a set of specific locational and environmental effects.

A. Impact of Tx and Rx Placement

The large set of O-I scenarios measured permits the isolation of certain environmental effects relating to the location of the BS or CPE, to understand the potential impacts on the measured path loss and azimuth beamforming gain.

1) Different Sides of an Elevated Subway Track: We observe differences in path loss not only between scenarios at different buildings, but also between scenarios on opposite sides of the same street. A notable example of this is shown for the JLG-N-W and JLG-N-E scenarios in Figs. 7(a) and 7(b). An elevated subway track bisects the two sides of the street; the receiver was placed at **JLG** directly in-line with JLG-N-W; JLG-N-E is the sidewalk on the far side of the street behind the subway track.

The path loss model for JLG-N-E in Fig. 7(a) is consistently 10 dB lower than the model for JLG-N-W over the distance covered. Furthermore, Fig. 7(b) shows the median azimuth beamforming gain for JLG-N-E is degraded by a further 1.8 dB, for a total median beamforming gain loss of almost 6 dB. This result indicates that the elevated subway tracks add a significant amount of path loss and scattering. We believe this scenario is a representative example of grade-separated urban transit, including elevated roadways or pedestrian bridges.

2) Different Floors of the Same Building: As a typical urban building occupies more than one floor, it is useful to understand the effect, if any, of the height of an indoor CPE. We use the measurements from **TEA** where the Rx was placed on the second and third floors, such that the Rx is at the same distance along the street, only higher or lower in elevation. The indoor layout of the second and third floors where the Rx is placed is largely identical, meaning any observed difference is due to the outdoors propagation environment. The Tx was then placed along identical locations on the street sidewalks. The results of this comparison can be seen in Fig. 7(c), which shows that the CPE experiences 8–10 dB lower path loss on the third floor than the second floor. Furthermore, Fig. 7(d) shows that the third floor experiences around 1 dB lower azimuth beamforming gain degradation.

We observe that the street sidewalks along **TEA** have trees planted at regular intervals. Therefore, a plausible explanation for this result is that the higher floor has a view of the Tx which experiences less blockage due to foliage. A lower blockage from foliage would also explain the lower azimuth beamforming gain degradation, as foliage can create significant scattering [18], [49].

3) Angle of Incidence: The measurement presented in Fig. 3 shows that the AoI into the window can have an over 10 dB impact on glass transmission loss, with the highest loss between 45° and 50°. In each O-I scenario, the Tx is moved perpendicular/parallel to the window by the Rx, leading to a normal/oblique AoI into the window. The Tx was moved in both ways during the measurements at **NWC**. As seen in Fig. 8, we group the **NWC** O-I scenarios without scaffolding, listed with “NSc” in Table III, according to the street geometry by considering the AoI of the straight line between the Tx and Rx. We generate two groups, one where $\text{AoI} < 45^\circ$, and the second where $\text{AoI} \geq 45^\circ$. For cases where LOS from Tx to Rx is blocked, the real AoI for the mmWave signal is difficult to determine. Hence we do not include any **NWC-N-E-*** or **NWC-W-S-*** measurements as they lose visual LOS to **NWC** as the Tx moves farther away.

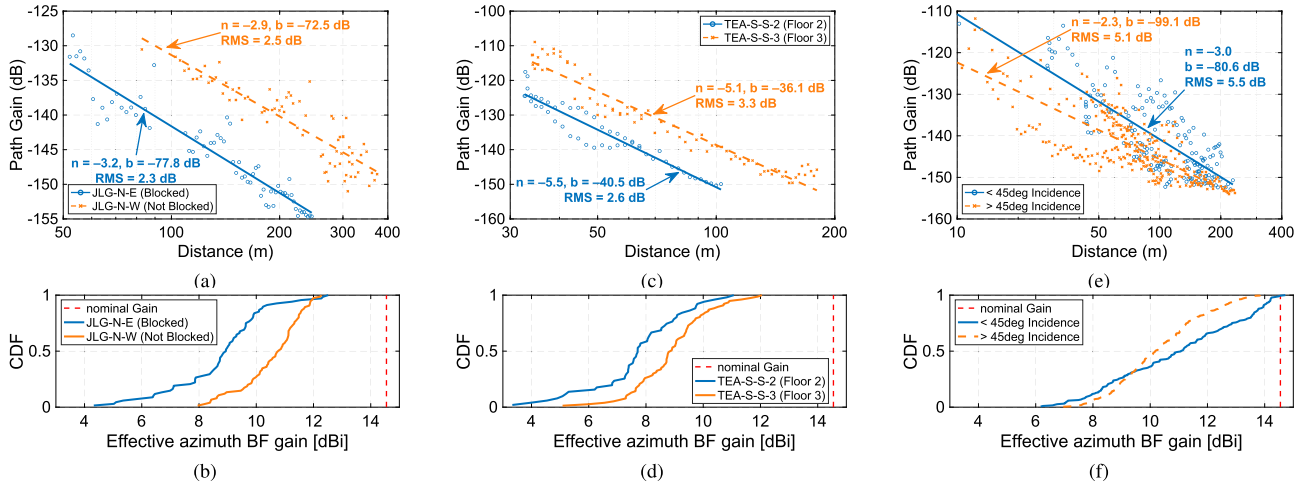


Fig. 7. Path gain and azimuth beamforming gain measurements for different placements of Tx and Rx: (a,b) Tx blocked or not blocked by a raised subway track measured from **JLG**, (c,d) Rx placed on different floors of **TEA**, and (e,f) AoI above or below 45° at **NWC**.

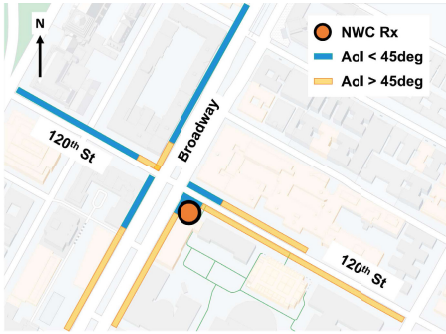


Fig. 8. Overview of AoI measurement grouping for six sidewalks at **NWC**. Tx locations on sidewalks marked in blue have less than 45° degrees incidence into the glass, those in orange have greater than 45° degrees incidence.

We observe up to a 9 dB difference between the best-fit models for the two groups at 50 m in Fig. 7(e), corresponding to the observed 10 dB range of glass transmission loss in Fig. 3. There is a smaller difference at greater distances; we expect this is due to greater scattering reducing the importance of the AoI for the direct shot between Tx and Rx. The azimuth beamforming plot in Fig. 7(f) shows that the median beamforming gain is around 1 dB lower for the higher AoI group, implying that O-I scenarios with a larger AoI experience not only a greater path loss but also a larger degree of scattering.

B. Effects of Foliage and Scaffolding

We consider repeated O-I scenarios where the only difference is a single environmental variable. As the measurement campaign was conducted over 20 months given the COVID-19 pandemic, we were able to collect measurements in the presence/absence of scaffolding and tree foliage.

1) Scaffolding: A common feature seen in urban environments is scaffolding, which typically encloses the sidewalk in front of a building for the purpose of supporting a work crew or protecting pedestrians from debris. BSes located on street lightpoles may lose direct LOS to CPEs in lower floors when scaffolding is present. In our campaign, we collected measurements from NWC-N-W and NWC-E-N one year apart, with and without scaffolding (noted by “Sc” or “NSc” for

NWC rows in Table III), which allowed us to isolate its effect. This scaffolding is visible in Fig. 9(a).¹

Fig. 9(c) shows that the presence of scaffolding leads to a uniform 5 dB additional path loss. This corresponds well to the 4-6 dB measurable penetration loss typical of pressed wood [48], which made up the majority of the scaffold which was located outside of NWC. Fig. 9(d) shows an additional 1 dB beamforming degradation with the presence of scaffolding, indicating that scaffolding introduces additional environmental scattering. These two results combined show that the common occurrence of scaffolding located directly outside of an indoors location can have a meaningful impact on the O-I link budget.

2) Presence of Tree Leaves: City streets are typically lined with trees. Foliage can have a notable impact on path loss [49] and foliage in NYC changes with the different seasons. In our campaign, we collect measurements from NWC-N-E, NWC-W-N, and NWC-W-S twice: once in the summer, with full tree leaf cover, and once in the winter, without tree leaves. These scenarios are named accordingly with “Le” and “NLE” in the NWC rows in Table III. As with the scaffolding comparison, all other variables in the environment were controlled to the greatest extent possible to ensure that the only difference is the presence of leaves on deciduous trees.

Fig. 9(e) shows a 2-3 dB increase in path loss when tree leaves are present. This relatively small increase is expected, as it is similar to observations in prior O-O measurements [19] in the same area. While there are trees at regular intervals on these sidewalks, they are typically not dense enough to significantly impact even visual LOS. The sidewalk trees present around NWC in Fig. 2 are typically young, small, and thin, as can be seen in Fig. 9(b). Therefore, if the street tree foliage has the aforementioned characteristics, only a relatively minor impact on the path loss is expected. However, Fig. 9(f) shows a 2-3 dB degradation in median azimuth beamforming gain when foliage is present, which is larger than the increased degradation with scaffolding, and is in line

¹TEA-S-N-1-Sc and TEA-S-S-1-Sc were also measured with scaffolding outside the window, but we were unable to measure them without scaffolding during the measurement campaign.

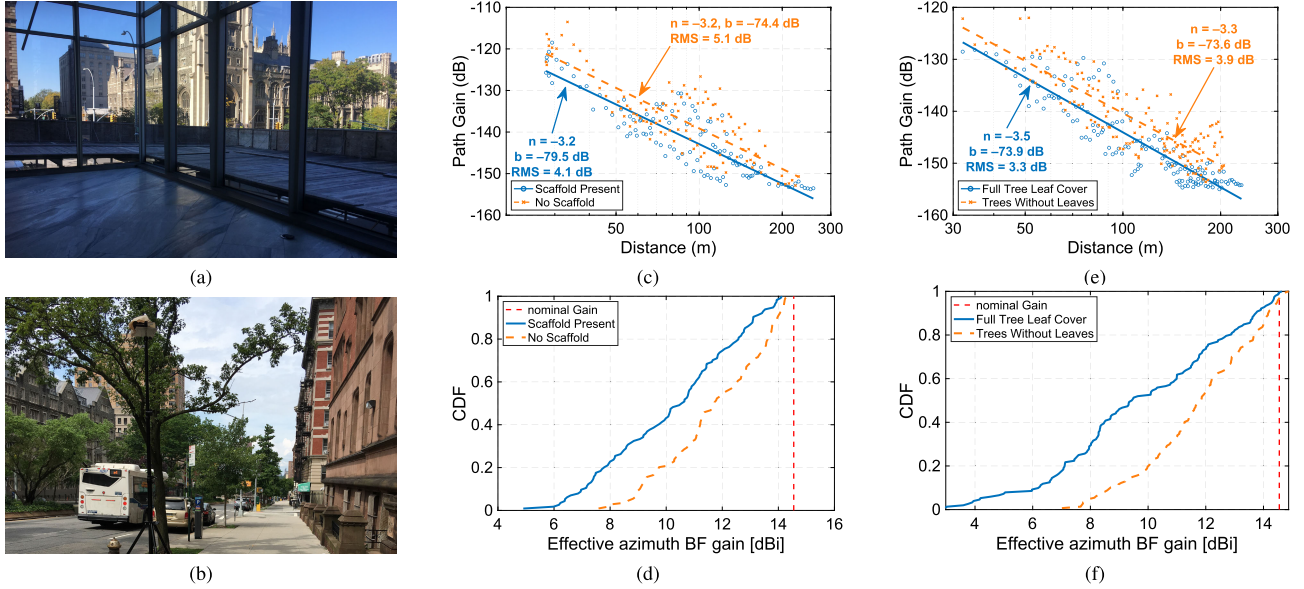


Fig. 9. Path gain and azimuth beamforming gain measurements for different environmental factors. (a) scaffolding present at NWC, (b) typical full tree leaf cover on the sidewalk used for scenario NWC-N-E, (c,d) scaffold/no scaffold measurements at NWC and (e,f) foliage/no foliage measurements at NWC.

with the understanding that foliage can introduce significant scattering [18], [49].

By combining the measured increases in path loss and beamforming gain degradation, we observe that the presence of scaffolding or tree leaves can each reduce the O–I mmWave link budget by 4–6 dB. This result is uniform over the five O–I scenarios considered from **NWC**. Due to the preponderance of these two factors in urban environments, their consideration is important in network planning for mmWave O–I coverage.

VII. CASE STUDY: A PUBLIC SCHOOL

In this section, we provide a detailed case study conducted at the Hamilton Grange Public School (**HMS**), which is located in Hamilton Heights (West Harlem) within the COSMOS testbed deployment area and the FCC Innovation Zone. According to the NYC Internet Master Plan [3], the COSMOS testbed deployment area, covering the neighborhoods of Manhattanville and Hamilton Heights with > 3,600 public housing units, is impacted by the digital divide. Up to 32% and 18% of the households in Manhattanville and Hamilton Heights, respectively, do not subscribe to home broadband service. On the other hand, according to [3], 80% and 43% of the Manhattanville and Hamilton Heights land areas, respectively, are geographically optimal for mmWave FWA. Therefore, conducting measurements at **HMS**, a representative building within its neighborhood, offers a unique opportunity to study the feasibility of using mmWave FWA as a broadband alternative in a real world environment.

As **HMS** uses traditional glass for its windows, it experiences a significantly lower path loss compared to the other measured locations, an effect detailed in Section V-B. Combined with the aforementioned general opportunity for FWA in the surrounding neighborhood, the low path loss makes **HMS** a location of particular interest. We analyze the measurements at **HMS** in classrooms which are mapped in Fig. 10(a) and enumerated in Table III, and a hallway mapped in Fig. 11(a).

We then compare path gain models for the individual classrooms and study how the mmWave signal propagates into the indoor hallway. *We shared the dataset from **HMS** via the NIST 5G Channel Model Alliance repository [36].* The models in Table III and results in Figs. 10 and Figs. 11 are reproducible from this dataset.

A. Classroom Measurements

Measurements at **HMS** were taken with the Rx located in five classrooms along the third floor of the school building. We note that the classrooms are all very regular in dimension as well as interior layout. The Tx was moved along two paths, one along the school parking lot located directly outside the classrooms, and the other along the basketball courts located at a greater distance. A map of the school and measurement locations, along with path gain results for the two Tx paths, are shown in Fig. 10.

The model fitted to all classroom measurements with the Tx located in the parking lot in Fig. 10(b) shows a slope of $n = 3.9$, and is within 4 dB agreement with the theoretical model [50, eq. (27)] (with plain glass windows of dimension 1.5×4 m) for direct-line O–I propagation from a BS located within a street canyon. The theoretical model, also shown in Fig. 10(b), shares the slope of $n = 3.9$ over a 40–90 m Tx–Rx distance. The measured path gain values from different classrooms largely overlap, an understandable result given the uniformity of the five classrooms considered. The relatively low 10–20 dB excess loss above free space in Fig. 6(a) indicates a strong potential for O–I coverage.

Similar results with the Tx located in the basketball court are shown in Fig. 10(c). Unlike the measurements with the Tx in the parking lot, there is some dependence on the classroom being measured. In particular, Room 307 has a noticeably higher path gain compared to the other classrooms. One possible reason is the row of trees visible near the middle of the map in Fig. 10(a). As seen from ground level at the

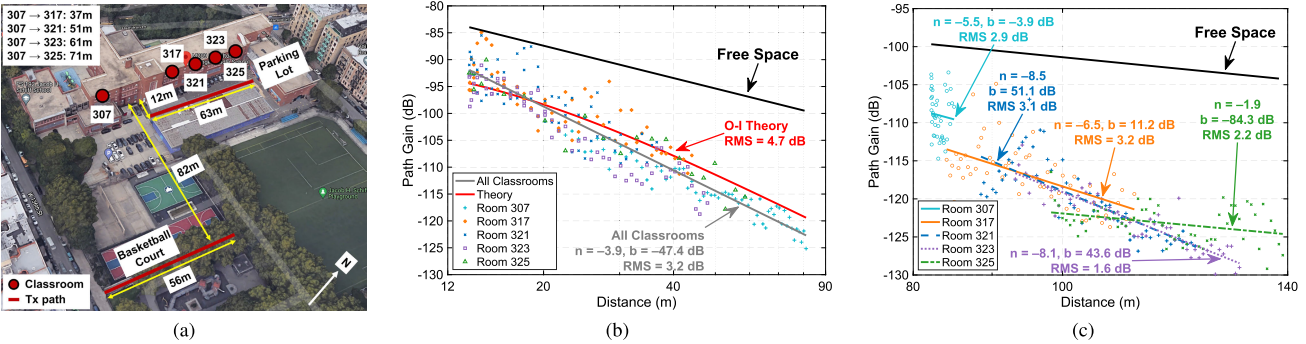


Fig. 10. Summary of path gain measurements taken at HMS. (a) Map of measurement locations. Maroon lines represent paths along which the channel sounder Tx was moved for each classroom Rx location, which correspond to entries in Table III. (b) Grouped path gain model for all classrooms along with theoretical model [50, eq. (27)] with the Tx placed along the parking lot directly outside the classrooms. (c) Per-classroom path gain models with the Tx placed along the basketball court. Distances represent the three-dimensional Euclidean distance between Tx and Rx.

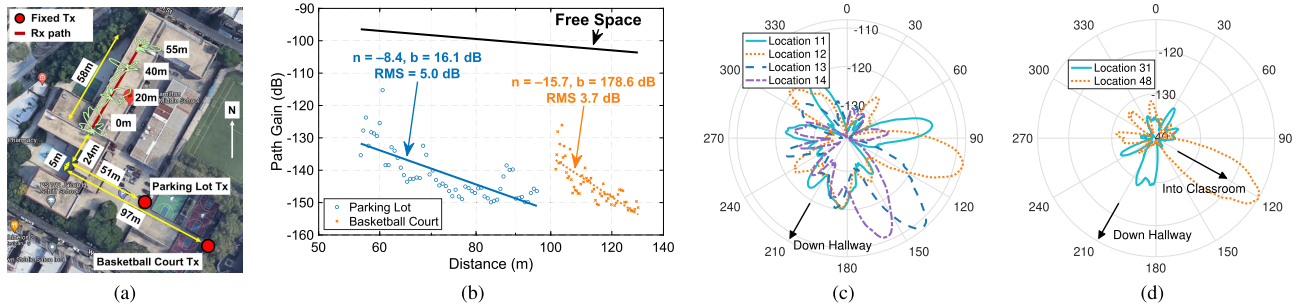


Fig. 11. Hallway measurements at HMS taken from two different Tx locations. (a) Map of the hallway measurements and example power angular spectra for the Tx located in the parking lot. (b) Path gain models for both Tx locations. (c) Successive angular spectra showing the peak angle rotating as the Rx moves past a classroom door, demonstrating the presence of a strong propagation path via the nearest classroom. (d) Two other angular spectra showing two different dominant propagation paths; one through a classroom, and one down the hallway.

basketball court, these trees did partially block the view of the windows for classrooms 317 to 325, which likely accounts for the higher loss experienced by these classrooms.

B. Hallway Measurements

Table IV lists two measurements taken by moving the Rx along an interior hallway located behind the row of classrooms indicated in Fig. 11(a). The Tx was kept in two fixed positions, one in the parking lot and the other at the basketball court, noted by the “Fixed Tx” locations in the same figure. The Rx was moved along the hallway in an identical manner for both Tx locations, leading to a total of 116 measurements taken of the interior hallway. The path gain and azimuth beamforming gain measurements are shown in Fig. 11.

The path gain results in Fig. 11(b) show a 5 dB difference between the two models, with the large n indicating a fast drop-off in received power as the Rx moves down the hallway. The plotted distance in Fig. 11(b) is the three-dimensional Euclidean distance from Rx to Tx; the Rx was moved along a 58 m linear distance down the hallway in both measurements. This distance is compressed within the three-dimensional Euclidean distance, creating the particularly steep slopes. Unlike the measurements in Table III, there was no direct LOS path from Tx to Rx. Indoor locations far from a window typically have several candidate propagation paths [51]. In the case of these hallway measurements, we consider two likely mechanisms [50]: (i) via the room most normal to the Tx, and (ii) via the room closest to the location of the Rx. We study the propagation mechanism by investigating the angular spectra $\bar{S}(d, \phi)$ measured at several Tx-Rx links.

Fig. 11(a) shows angular spectra for different Rx locations along the hallway. The spectra lack a persistent dominant direction along the hallway which would be characteristic of propagation mechanism (i). Fig. 11(c) shows how the peak angle rotates as the Rx moves past the doorway of Room 317, where locations {11, 12} and {13, 14} are on either side of the doorway. Here, mechanism (ii) is dominant and the Rx receives a signal through the doorway of Room 317; this effect was observed for Rx locations close to other classroom doors as well. The angular spectra in Fig. 11(d) show that some Rx locations receive a signal peak from down the hallway via Room 307, the room most normal to the Tx (propagation mechanism (i)). As these results align with the theory [50], [51], the typicality of HMS suggests that for buildings with low-loss glass and windows overlooking the BS, the dominant propagation path into a hallway will be via the nearest doorway from a room with such a window.

VIII. GLASS-DEPENDENT O-I CAPACITY & COVERAGE

The models in Section V-B are now used to develop a measure of achievable link capacity for O-I scenarios with “traditional” or Low-e glass. Table V defines typical parameters for the 28GHz BS and CPE representative of recent advances in state-of-the art mmWave hardware [52], [53], [54], [55], [56]. We select conservative values for these parameters to reduce the possibility of overestimating data rates, and we include an additional 5 dB of losses in NF to bring it to 9 dB. The resulting Rx noise floor is $N = -174 + 10 \log_{10} B + NF = -76$ dBm. In this analysis, we assume that the BS

TABLE V

TYPICAL DEVICE PARAMETERS FOR A 28 GHz TX (BS) AND RX (CPE)

Quantity	Symbol	Value	Ref.
Tx Power	P_{Tx}	+28 dBm	[52]
Tx Antenna Gain	G_{Tx}	23 dBi	[52]
Rx Antenna Gain	G_{Rx}	23 dBi	[52], [63]
Rx Noise Figure	NF	9 dB	[55]
Bandwidth	B	800 MHz	[52], [56]

and CPE are able to correctly align their transmit and receive beams [57], [58], and that the CPE is located one meter from the window, as the Rx was during the measurements.

As the signal-to-noise (SNR) will determine the achievable capacity, we present a relevant measure of data rate coverage by considering the 10th percentile $SNR(d)$, $SNR_{10}(d)$, which defines the SNR that 90% of CPEs will exceed. The SNR in dB may be computed as $SNR(d) = P_{Tx} + G_{Tx} + G_{Rx} - G_{deg}(d) + G_{path}(d) - N$, where $G_{path}(d)$ is computed from our path gain model. $G_{deg}(d)$ is computed as the sum (in dBi) of two values: (i) the median empirically measured azimuth beamforming gain degradation, and (ii) the zenith degradation computed from practical values for angular spread in zenith provided by 3GPP [43]. The distribution of SNR arises from the RMS error in the slope-and-intercept models used, which represents the channel shadow fading.

Given an empirical path gain model M , we can represent the SNR as a normally distributed random variable $SNR \sim \mu(M) + \sigma(M) \cdot \mathcal{N}(0, 1)$, where μ and σ are the mean and standard deviation of M , respectively. M is itself a function of d , therefore a normally distributed SNR random variable is defined for every distance d .

We consider three SNR boundaries: 25 dB, 14 dB, and 4 dB. These represent minimum SNRs at which 256QAM 4/5, 16QAM 1/2, and QPSK 3/10 modulation and coding schemes (MCS) become advantageous to use [59], [60], [61]. We employ an impaired Shannon downlink capacity $\hat{R} = \rho\beta B \log_2(1 + 10^{(SNR-C)/10})$, where $\rho = 0.6$ is the overhead factor, $\beta = 0.8$ is the time-division duplexing downlink ratio, and $C = 3$ dB is implementation loss. This leads to realistically impaired downlink capacities of $\hat{R} = 2.8, 1.4$, and 0.4 Gb/s for SNRs corresponding to 256QAM, 16QAM, and QPSK respectively. These are close to values from 3GPP [59], [60]; we note that these represent conservative upper bounds for achievable downlink throughput. The evaluation of achievable throughput is a subject of our future research, utilizing the full communication stack provided by the mmWave phased array antennas integrated in the COSMOS testbed [35], [62].

A. Buildings with Traditional Glass

As shown in Sections V-B and VII, buildings with “traditional” glass experience lower path loss, suggesting a strong potential for O-I coverage at 28 GHz. From Fig. 6(a), we set the slope $n = 3$, intercept $b = -59.8$ dB, and $\sigma = 4.3$ dB. For each outdoor link distance $d \in \{10, 11, \dots, 200\}$, we compute the 10th percentile path gain given by the log-normal distribution $G_{path,i}(d) = b + n \cdot 10 \log_{10} d + \sigma \cdot \mathcal{N}(0, 1)$. We also compute the median total beamforming gain degradation $G_{deg,i} = 14.5 - G_{az,m} + 3.5$ where $G_{az,m}$ is the median of

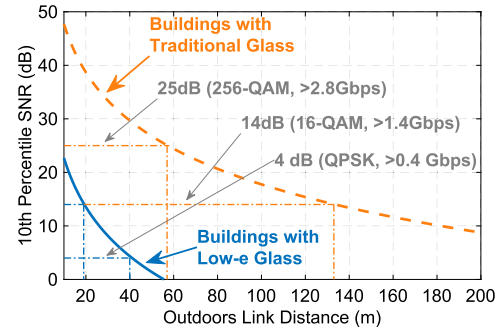


Fig. 12. 10th percentile SNR predictions for buildings with Low-e or traditional glass windows, with coverage ranges d^* marked for various MCS.

the azimuth beamforming gain distribution for traditional glass in Fig. 6(b), 14.5 is the gain of the Rx antenna in azimuth, and 3.5 is the degradation in zenith beamforming gain caused by 10° angular spread. This leads to a total degradation of 7 dB.

The top curve in Fig. 12 demonstrates $SNR_{10}(d) > 25$ dB for $d \leq 57$ m, meaning that 256-QAM modulation is supported for at least 90% of indoor CPEs at a link distance of up to 57 m. This corresponds to $\hat{R} > 2.8$ Gb/s. 16-QAM 1/2 MCS for 90% of indoor CPEs is supported up to 133 m, corresponding to $\hat{R} > 1.4$ Gb/s. While not shown in Fig. 12, QPSK 3/10 is supported for 90% of indoor CPEs at a BS distance of 288 m, corresponding to $\hat{R} > 0.4$ Gb/s.

These measurements covered a variety of Tx and Rx locations at **HMS** as shown in Fig. 10(a), with many links occluded by foliage and with a large variation in the AoI. Thus, we believe these results to be representative of building constructions with traditional glass in typical urban environments.

B. Buildings with Low-e Glass

We repeat the SNR calculations using the Low-e model in Fig. 6(a), setting $n = 3$, $b = -79.6$ dB, and $\sigma = 8.4$ dB, producing the lower curve of Fig. 12. The results show that 256-QAM coverage cannot be supported for at least 90% of CPEs even at the shortest realistic Tx-Rx link distance. Instead, 16-QAM 1/2 ($\hat{R} > 1.4$ Gb/s) and QPSK 3/10 ($\hat{R} > 0.4$ Gb/s) MCS may be supported up to 19 m and 40 m, respectively. As the Low-e glass model uses data from six different buildings, we believe this result is representative of buildings with Low-e glass in an urban environment.

While indoor coverage potential is significantly higher for buildings with older, thinner glass, coverage at gigabit data rates is still feasible even in buildings with modern construction if the BS is nearby (~20 m). This suggests the benefit of considering glass type during network planning.

IX. ANGULAR SEPARATION OF INDOOR USERS

The ability to utilize multiple spatial streams through the use of beamforming and beamsteering with a single [64] or multiple antennas can enhance data rates in mmWave networks [65], [66], [67], [68]. This may help the heavily inhibited downlink capacity demonstrated in Section VIII for O-I scenarios with Low-e glass. However, in the presence of multiple users, inter-user-interference (IUI) caused by low angular separation

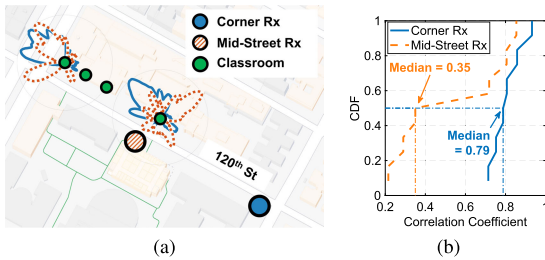


Fig. 13. Measurements at TEA with Tx and Rx reversed. (a) Map of Rx locations on the balcony and angular spectra overlaid on select Tx locations. (b) CDF of correlation coefficient between power angular spectra.

adds further challenges to providing coverage. In this section, we evaluate the angular separation of indoors users at **TEA** from the perspective of a BS placed at two different outdoors locations: (i) at the street corner and (ii) mid-block.

These two O-I scenarios at **TEA** are listed in Table IV. As the intention is to measure the direction of received power at the BS for different indoor user locations, we swapped the locations of the Tx and Rx compared to the scenarios in Table III. The Rx is placed on two outdoor balconies at the street corner and mid-way along the street, as shown in Fig. 13(a), where it emulates a BS. The Rx measures the received signal direction from the indoor Tx, which is moved between four different rooms at **TEA**.

The peak of the power angular spectra $\bar{S}(d, \phi)$ in Fig. 13(a) rotates as the Tx moves between rooms. Should this rotation be significant, the beams from different rooms will not overlap, producing lower IUI between users in different rooms. To quantify this effect, we compute the cross-correlation of $\bar{S}(d, \phi)$ (on the linear scale) across all pairs of rooms without repetition to form an estimate of the IUI, IUI_{ij} , between users at distances d_i and d_j :

$$IUI_{ij} = \frac{\langle \bar{S}(d_i, \phi), \bar{S}(d_j, \phi) \rangle}{|\bar{S}(d_i, \phi)| \cdot |\bar{S}(d_j, \phi)|}. \quad (5)$$

CDFs showing the distribution of IUI_{ij} for the two Rx locations are shown in Fig. 13(b). The CDF for the corner Rx location shows a high median IUI_{ij} of 0.79, likely caused by the similar incidence angles for the rooms located at the far end of the street. This indicates a high level of IUI. The mid-street Rx location has a much lower median IUI_{ij} of 0.35, which is likely due to the larger angular separation between Tx locations. These results indicate that a BS placed at a street corner, which is typically excellent for O-O USCM coverage, may be challenged when serving multiple indoors users. This arises due to the combination of high O-I path loss and higher IUI caused by lower angular separation between users.

X. CONCLUSION

We addressed the lack of extensive O-I mmWave measurements by conducting a large-scale measurement campaign consisting of over 2,200 Tx-Rx links across seven building sites in West Harlem, NYC. We used the measurements to develop single-slope exponent models for O-I path gain under various conditions. Among other things, these models show that downlink capacity in excess of 2.8 Gb/s is achievable for at least 90% of indoor CPEs located one meter from the

window in buildings with “traditional” glass and lightpole BS deployments at distances up to 57 m away. Capacity in excess of 1.4 Gb/s can be achieved by a BS up to 133 m away. Similar lightpole deployments up to 40 m range are capable of providing capacity in excess of 400 Mb/s for CPEs in buildings that use modern Low-e glass. We expect these results to inform the planning and deployment of mmWave networks, especially in urban areas with low Internet access, thereby helping to improve connectivity and bridging the digital divide. To accompany key results, we also make the **HMS** public school dataset publicly available via the NIST NextG Channel Model Alliance repository [36].

While we show that high link capacity and hence data rates for O-I scenarios is achievable, we also show how low angular separation between multiple indoors users from the outdoors BS can lead to additional challenges in supporting those users, with potentially high IUI. This illustrates the need for careful design of beamforming algorithms which take O-I scenarios into account. We will study this in future work using the 28 GHz phased array antenna modules integrated in the COSMOS Testbed [62] to implement and test the designed algorithms and evaluate the actual obtained data rates as well as take wideband channel measurements for other important results, such as the delay spread.

ACKNOWLEDGMENT

The authors thank A. D. Estigarribia and Z. Zheng for their help with the measurements. They also thank B. Masood, T. Riccio, J. Govan, and B. Han for their support during the measurement campaigns with **HMS**, **MIL**, **TEA**, and **JLG**. They also thank T. Chen for his helpful suggestions.

REFERENCES

- [1] M. Kohli et al., “Outdoor-to-indoor 28 GHz wireless measurements in manhattan: Path Loss, location impacts, and 90% coverage,” in *Proc. 23rd Int. Symp. Theory, Algorithmic Found. Protocol Des. Mobile Netw. Mobile Comput.*, Oct. 2022, pp. 201–210.
- [2] FCC. (2021). *Notes from the FCC: Addressing the Homework Gap*. [Online]. Available: <https://www.fcc.gov/news-events/notes/2021/02/01/addressing-homework-gap>
- [3] NYC Mayor’s Office of the CTO. (2020). *The New York City Internet Master Plan*. [Online]. Available: https://www1.nyc.gov/assets/cto/downloads/internet-master-plan/NYC_IMP_1.7.20_FINAL-2.pdf,
- [4] M. Polese, F. Restuccia, and T. Melodia, “DeepBeam: Deep waveform learning for coordination-free beam management in mmWave networks,” in *Proc. 22nd Int. Symp. Theory, Algorithmic Found. Protocol Design Mobile Netw. Mobile Comput.*, Jul. 2021, pp. 61–70.
- [5] Z. L. Fazliu, C. F. Chiasserini, F. Malandrino, and A. Nordio, “Graph-based model for beam management in mmWave vehicular networks,” in *Proc. 20st Int. Symp. Theory, Algorithmic Found. Protocol Design Mobile Netw. Mobile Comput.*, Oct. 2020, pp. 363–367.
- [6] S. G. Sanchez, S. Mohanti, D. Jaisinghani, and K. R. Chowdhury, “Millimeter-wave base stations in the sky: An experimental study of UAV-to-ground communications,” *IEEE Trans. Mobile Comput.*, vol. 21, no. 2, pp. 644–662, Feb. 2022.
- [7] S. Aggarwal, U. S. Sardesai, V. Sinha, D. D. Mohan, M. Ghoshal, and D. Koutsonikolas, “LiBRA: Learning-based link adaptation leveraging PHY layer information in 60 GHz WLANs,” in *Proc. 16th Int. Conf. Emerg. Netw. Exp. Technol.*, Nov. 2020, pp. 245–260.
- [8] Z. He, S. Mao, S. Kompella, and A. Swami, “On link scheduling in dual-hop 60-GHz mmWave networks,” *IEEE Trans. Veh. Technol.*, vol. 66, no. 12, pp. 11180–11192, Dec. 2017.

- [9] I. Khan, M. Ghoshal, S. Aggarwal, D. Koutsonikolas, and J. Widmer, "Multipath TCP in smartphones equipped with millimeter wave radios," in *Proc. 15th ACM Workshop Wireless Netw. Testbeds Exp. Evaluation Characterization*, Jan. 2022, pp. 54–60.
- [10] S. Aggarwal, S. K. Saha, I. Khan, R. Pathak, D. Koutsonikolas, and J. Widmer, "MuSher: An agile multipath-TCP scheduler for dual-band 802.11ad/AC wireless LANs," *IEEE/ACM Trans. Netw.*, vol. 30, no. 4, pp. 1879–1894, Aug. 2022.
- [11] D. Chizhik, J. Du, R. Feick, M. Rodriguez, G. Castro, and R. A. Valenzuela, "Path loss and directional gain measurements at 28 GHz for non-line-of-sight coverage of indoors with corridors," *IEEE Trans. Antennas Propag.*, vol. 68, no. 6, pp. 4820–4830, Jun. 2020.
- [12] V. Raghavan et al., "Millimeter-wave MIMO prototype: Measurements and experimental results," *IEEE Commun. Mag.*, vol. 56, no. 1, pp. 202–209, Jan. 2018.
- [13] K. Du, O. Ozdemir, F. Erden, and I. Guvenc, "28 GHz indoor and outdoor propagation measurements and analysis at a regional airport," in *Proc. IEEE 32nd Annu. Int. Symp. Pers. Indoor Mobile Radio Commun. (PIMRC)*, Sep. 2021, pp. 866–872.
- [14] S. Y. Jun et al., "Penetration loss at 60 GHz for indoor-to-indoor and outdoor-to-indoor mobile scenarios," in *Proc. 14th Eur. Conf. Antennas Propag. (EuCAP)*, Mar. 2020, pp. 1–5.
- [15] J. Senic et al., "Challenges for 5G and beyond," in *Proc. 16th Eur. Conf. Antennas Propag. (EuCAP)*, Mar. 2022, pp. 1–5.
- [16] H. Zhao et al., "28 GHz millimeter wave cellular communication measurements for reflection and penetration loss in and around buildings in new York city," in *Proc. IEEE Int. Conf. Commun. (ICC)*, Jun. 2013, pp. 5163–5167.
- [17] M. Z. Aslam, Y. Corre, J. Belschner, G. S. Arockiaraj, and M. Jäger, "Analysis of 60-GHz in-street backhaul channel measurements and LiDAR ray-based simulations," in *Proc. 14th Eur. Conf. Antennas Propag. (EuCAP)*, Mar. 2020, pp. 1–5.
- [18] J. Du, D. Chizhik, R. Feick, M. Rodríguez, G. Castro, and R. A. Valenzuela, "Suburban fixed wireless access channel measurements and models at 28 GHz for 90% outdoor coverage," *IEEE Trans. Antennas Propag.*, vol. 68, no. 1, pp. 411–420, Jan. 2020.
- [19] T. Chen et al., "28 GHz channel measurements in the COSMOS testbed deployment area," in *Proc. 3rd ACM Workshop Millim.-Wave Netw. Sens. Syst.*, Oct. 2019, pp. 39–44.
- [20] Y. Xing and T. S. Rappaport, "Propagation measurement system and approach at 140 GHz-moving to 6G and above 100 GHz," in *Proc. IEEE Global Commun. Conf. (GLOBECOM)*, Dec. 2018, pp. 1–6.
- [21] J. Ko et al., "Millimeter-wave channel measurements and analysis for statistical spatial channel model in-building and urban environments at 28 GHz," *IEEE Trans. Wireless Commun.*, vol. 16, no. 9, pp. 5853–5868, Sep. 2017.
- [22] K. Du et al., "60 GHz outdoor propagation measurements and analysis using Facebook terragraph radios," in *Proc. IEEE Radio Wireless Symp. (RWS)*, Jan. 2022, pp. 156–159.
- [23] M. Samimi et al., "28 GHz angle of arrival and angle of departure analysis for outdoor cellular communications using steerable beam antennas in new York city," in *Proc. IEEE 77th Veh. Technol. Conf. (VTC)*, Jun. 2013, pp. 1–6.
- [24] A. Shkel, A. Mehrabani, and J. Kusuma, "A configurable 60GHz phased array platform for multi-link mmWave channel characterization," in *Proc. IEEE Int. Conf. Commun. Workshops (ICC)*, Jun. 2021, pp. 1–6.
- [25] Y. Xing and T. S. Rappaport, "Millimeter wave and terahertz urban microcell propagation measurements and models," *IEEE Commun. Lett.*, vol. 25, no. 12, pp. 3755–3759, Dec. 2021.
- [26] Y. Zhang et al., "Improving millimeter-wave channel models for suburban environments with site-specific geometric features," in *Proc. Int. Appl. Comput. Electromagn. Soc. Symp. (ACES)*, Mar. 2018, pp. 1–2.
- [27] A. Narayanan et al., "A first look at commercial 5G performance on smartphones," in *Proc. Web Conf.*, Apr. 2020, pp. 894–905.
- [28] O. H. Koymen, A. Partyka, S. Subramanian, and J. Li, "Indoor mm-wave channel measurements: Comparative study of 2.9 GHz and 29 GHz," in *Proc. IEEE Global Commun. Conf. (GLOBECOM)*, Dec. 2015, pp. 1–6.
- [29] NIST Communications Technology Laboratory. (2022). *NextG Channel Model Alliance*. [Online]. Available: <https://www.nist.gov/ctl/nextg-channel-model-alliance>
- [30] C. A. L. Diakhate, J.-M. Conrat, J.-C. Cousin, and A. Sibille, "Millimeter-wave outdoor-to-indoor channel measurements at 3, 10, 17 and 60 GHz," in *Proc. 11th Eur. Conf. Antennas Propag. (EUCAP)*, Mar. 2017, pp. 1798–1802.
- [31] N. Ntetsikas et al., "60 GHz outdoor to indoor (O2I) propagation measurements in a university campus," in *Proc. IEEE 23rd Int. Workshop Signal Process. Adv. Wireless Commun. (SPAWC)*, Jul. 2022, pp. 1–5.
- [32] C. U. Bas et al., "Outdoor to indoor penetration loss at 28 GHz for fixed wireless access," in *Proc. IEEE Int. Conf. Commun. (ICC)*, May 2018, pp. 1–6.
- [33] C. Larsson, F. Harrysson, B.-E. Olsson, and J.-E. Berg, "An outdoor-to-indoor propagation scenario at 28 GHz," in *Proc. 8th Eur. Conf. Antennas Propag. (EuCAP)*, Apr. 2014, pp. 3301–3304.
- [34] FCC. (2021). *FCC Established two New Innovation Zones in Boston and Raleigh*. [Online]. Available: <https://www.fcc.gov/document/fcc-established-two-new-innovation-zones-boston-and-raleigh>
- [35] D. Raychaudhuri et al., "Challenge: COSMOS: A city-scale programmable testbed for experimentation with advanced wireless," in *Proc. 26th Annu. Int. Conf. Mobile Comput. Netw.*, Apr. 2020, pp. 1–13.
- [36] M. Kohli and A. Adhikari. (2022). *28GHz Outdoor-Indoor West Harlem NYC Public School Dataset*. [Online]. Available: <https://nextg.nist.gov/submissions/131>
- [37] D. Chizhik, J. Du, R. Valenzuela, A. Bedin, M. Moisio, and R. Feick, "Measured and modeled outdoor indoor coverage at 28 GHz into high thermal efficiency buildings," in *Proc. IEEE Int. Symp. Antennas Propag. USNC-USRI Radio Sci. Meeting (USNC-USRI)*, Jul. 2023, pp. 405–406.
- [38] K. A. Remley et al., "Measurement challenges for 5G and beyond: An update from the national institute of standards and technology," *IEEE Microw. Mag.*, vol. 18, no. 5, pp. 41–56, Jul. 2017.
- [39] M. Schmieder, M. Peter, R. Askar, I. Komsic, and W. Keusgen, "Measurement and characterization of 28 GHz high-speed train backhaul channels in rural propagation scenarios," in *Proc. 12th Eur. Conf. Antennas Propag. (EuCAP)*, Apr. 2018, pp. 1–5.
- [40] (2021). *IEEE 802.11ay-2021-IEEE Standard for Information Technology*. [Online]. Available: https://standards.ieee.org/standard/802_11ay-2021.html
- [41] NYC Dept., of Information Technology & Telecommunications. (2022). *5G Rollout*. [Online]. Available: <https://www1.nyc.gov/site/doitt/business/5g-design/5g.page>
- [42] Samsung. (2022). *Compact Macro (Access Unit)* [Online]. Available: <https://www.samsung.com/global/business/networks/products/radio-access/access-unit/>
- [43] *Study on Channel Model for Frequencies*, Standard 3GPP TR 38.901 Version 17.0.0 Release 17, 3GPP, 2022. [Online]. Available: https://www.etsi.org/deliver/etsi_tr/138900_138999/138901/17.00.00_60/tr_138901v170000p.pdf
- [44] L. J. Greenstein, D. G. Michelson, and V. Erceg, "Moment-method estimation of the Ricean K-factor," *IEEE Commun. Lett.*, vol. 3, no. 6, pp. 175–176, Jun. 1999.
- [45] New York State Department of Transportation. (2019). *Traffic Data Viewer*. [Online]. Available: <https://www.dot.ny.gov/tdv>
- [46] K. Du, O. Ozdemir, F. Erden, and I. Guvenc, "Sub-terahertz and mmWave penetration loss measurements for indoor environments," in *Proc. IEEE Int. Conf. Commun. Workshops (ICC Workshops)*, Jun. 2021, pp. 1–6.
- [47] H. Kim and S. Nam, "Transmission enhancement methods for low-emissivity glass at 5G mmWave band," *IEEE Antennas Wireless Propag. Lett.*, vol. 20, no. 1, pp. 108–112, Jan. 2021.
- [48] C. Vargas, L. da Silva Mello, and R. C. Rodriguez, "Measurements of construction materials penetration losses at frequencies from 26.5 GHz to 40 GHz," in *Proc. IEEE PACRIM*, 2017, pp. 1–4.
- [49] S. Yang, J. Zhang, and J. Zhang, "Impact of foliage on urban mmWave wireless propagation channel: A ray-tracing based analysis," in *Proc. Int. Symp. Antennas Propag. (ISAP)*, Oct. 2019, pp. 1–3.
- [50] D. Chizhik, J. Du, and R. A. Valenzuela, "Universal path gain laws for common wireless communication environments," *IEEE Trans. Antennas Propag.*, vol. 70, no. 4, pp. 2928–2941, Apr. 2022.
- [51] D. Shakya, D. Chizhik, J. Du, R. A. Valenzuela, and T. S. Rappaport, "Dense urban outdoor-indoor coverage from 3.5 to 28 GHz," in *Proc. ICC - IEEE Int. Conf. Commun.*, May 2022, pp. 932–937.
- [52] B. Sadhu et al., "A 28-GHz 32-element TRX phased-array IC with concurrent dual-polarized operation and orthogonal phase and gain control for 5G communications," *IEEE J. Solid-State Circuits*, vol. 52, no. 12, pp. 3373–3391, Dec. 2017.
- [53] Z. Deng, J. Zhou, H. J. Qian, and X. Luo, "A 22.9–38.2-GHz dual-path noise-canceling LNA with 2.65–4.62-dB NF in 28-nm CMOS," *IEEE J. Solid-State Circuits*, vol. 56, no. 11, pp. 3348–3359, Nov. 2021.

- [54] I.-J. Hwang, J.-I. Oh, H.-W. Jo, K.-S. Kim, J.-W. Yu, and D.-J. Lee, "28 GHz and 38 GHz dual-band vertically stacked dipole antennas on flexible liquid crystal polymer substrates for millimeter-wave 5G cellular handsets," *IEEE Trans. Antennas Propag.*, vol. 70, no. 5, pp. 3223–3236, May 2022.
- [55] A. Ershadi, S. Palermo, and K. Entesari, "A 22.2–43 GHz gate-drain mutually induced feedback low noise amplifier in 28-nm CMOS," in *Proc. IEEE Radio Freq. Integr. Circuits Symp. (RFIC)*, Jun. 2021, pp. 27–30.
- [56] Y.-W. Chang, T.-C. Tsai, J.-Y. Zhong, J.-H. Tsai, and T.-W. Huang, "A 28 GHz linear and efficient power amplifier supporting wideband OFDM for 5G in 28nm CMOS," in *IEEE MTT-S Int. Microw. Symp. Dig.*, Aug. 2020, pp. 1093–1096.
- [57] S. Sur, I. Pefkianakis, X. Zhang, and K.-H. Kim, "Towards scalable and ubiquitous millimeter-wave wireless networks," in *Proc. 24th Annu. Int. Conf. Mobile Comput. Netw.*, Oct. 2018, pp. 257–271.
- [58] M. S. Zia, D. M. Blough, and M. A. Weitnauer, "Effects of SNR-dependent beam alignment errors on millimeter-wave cellular networks," *IEEE Trans. Veh. Technol.*, vol. 71, no. 5, pp. 5216–5230, May 2022.
- [59] Study on Support of NR Downlink 256 Quadrature Amplitude Modulation (QAM) for Frequency Range 2 (FR2), Standard ATIS.3GPP.38.883.V1600, ATIS 3GPP, 2020. [Online]. Available: <https://www.atis.org/wp-content/uploads/3gpp-documents/Rel16/ATIS.3GPP.38.883.V1600.pdf>
- [60] User Equipment (UE) Conformance Specification; Radio Transmission and Reception, Standard 3GPP TS 38.521-4 Version 15.0.0 Release 15, 3GPP, 2019. [Online]. Available: https://www.etsi.org/deliver/etsi_ts/138500_138599/13852104/15.00.00_60/ts_13852104v150000p.pdf
- [61] E. Peralta et al., "5G new radio base-station sensitivity and performance," in *Proc. 15th Int. Symp. Wireless Commun. Syst. (ISWCSS)*, Aug. 2018, pp. 1–6.
- [62] T. Chen et al., "Open-access millimeter-wave software-defined radios in the PAWR COSMOS testbed: Design, deployment, and experimentation," *Comput. Netw.*, vol. 234, Oct. 2023, Art. no. 109922.
- [63] Qualcomm. (2021). QTM547 mmWave Antenna Module. [Online]. Available: https://www.qualcomm.com/content/dam/qcomm-martech/dm-assets/documents/prod_brief_qcom_qtm547.pdf
- [64] Y. Aslan, S. Salman, J. Puskely, A. Roederer, and A. Yarovoy, "5G multi-user system simulations in Line-of-Sight with space-tapered cellular base station phased arrays," in *Proc. 13th Eur. Conf. Antennas Propag. (EuCAP)*, Mar. 2019, pp. 1–5.
- [65] I. K. Jain, R. Subbaraman, and D. Bharadia, "Two beams are better than one: Towards reliable and high throughput mmWave links," in *Proc. ACM SIGCOMM Conf.*, Aug. 2021, pp. 488–502.
- [66] Y. Ghasempour, M. K. Haider, C. Cordeiro, D. Koutsonikolas, and E. Knightly, "Multi-stream beam-training for mmWave MIMO networks," in *Proc. 24th Annu. Int. Conf. Mobile Comput. Netw.*, Oct. 2018, pp. 225–239.
- [67] J. Zhao and X. Wang, "On the efficiency of multi-beam medium access for millimeter-wave networks," *IEEE/ACM Trans. Netw.*, vol. 30, no. 4, pp. 1469–1480, Aug. 2022.
- [68] Y. Yang et al., "MDSR: Multi-dimensional spatial reuse enhancement for directional millimeter-wave wireless networks," *IEEE Trans. Mobile Comput.*, vol. 21, no. 12, pp. 4439–4455, Dec. 2022.



Manav Kohli (Student Member, IEEE) received the Sc.B. degree (magna cum laude) in electrical engineering from Brown University in 2018. He is currently pursuing the Ph.D. degree in electrical engineering with the Wireless and Mobile Networking Laboratory (WiMNet), Columbia University. His research focuses on technologies for future wireless networks, including full-duplex wireless, millimeter-wave, and testbeds for open-access wireless experimentation, such as the NSF PAWR COSMOS testbed in West Harlem, New York City. His work was supported by the NSF Graduate Research Fellowship Program and the National Physical Science Consortium's Graduate Fellowships for STEM Diversity.



Abhishek Adhikari received the B.S. degree (magna cum laude) in computer engineering from Drexel University in 2021. He is currently pursuing the combined M.S./Ph.D. degrees with the Department of Electrical Engineering, Columbia University. His research is on wireless communication and sensing, with a focus on path loss modeling and micro-climate prediction using millimeter-wave. He was a recipient of the Columbia Evergreen Fellowship in 2021.



Gulnur Avci received the B.S. degree in electrical engineering from Columbia University in 2023. She was with the WiMNet Laboratory in Summer 2021, focusing on mmWave channel measurements within the COSMOS testbed deployment area. She was an Intern with the NASA Glenn Research Center in Fall 2021 and completed an internship with the HRL Laboratories in Summer 2022.



Sienna Brent received the B.S. degree in electrical engineering from Columbia University in 2023. She is currently a System Development Engineer with Amazon Web Services (AWS). She worked on mmWave channel measurements with the WiMNet Laboratory in Summer 2021. She has completed an internship with the T-Mobile RF Engineering Team based in New York City in Fall 2021 and completed an internship with AWS in Summer 2022.



Aditya Dash received the B.S. degree in electrical engineering from the University of Maryland and the M.S. degree in electrical engineering from Columbia University. He was with the WiMNet Laboratory, Columbia, in Fall 2022, worked on mmWave channel measurements at 28 and 60 GHz. He was a Software Developer with Intelsat prior to starting the M.S. program. Currently, he is a Junior Communications Engineer with AMERGINT.



Jared Moser graduated from Stuyvesant High School in 2022. He is currently pursuing the B.S. degree in mechanical engineering, with a focus on materials and manufacturing with Johns Hopkins University. He is a member of the Weihs Laboratory, working on the characterization of reactive metallic powders. While at Stuyvesant, he was with the WiMNet Laboratory, worked on mmWave and sub-6 GHz channel measurements in Summer 2021 and Summer 2022.



Sabbir Hossain (Student Member, IEEE) is currently pursuing the bachelor's degree in electrical engineering with The City College of New York. He was a recipient of the Amazon SURE Award in Summer 2021, under which he performed research into the wireless channel at mmWave and sub-6 GHz within the COSMOS testbed deployment area.



Igor Kadota (Member, IEEE) received the B.S. degree in electronic engineering and the first S.M. degree in telecommunications from the Aeronautics Institute of Technology (ITA), Brazil, in 2010 and 2013, respectively, and the second S.M. and Ph.D. degrees in communication networks from the Massachusetts Institute of Technology (MIT) in 2016 and 2020, respectively.

He is an Assistant Professor with the Department of Electrical and Computer Engineering, Northwestern University. He was a Post-Doctoral Research Scientist with Columbia University, from 2020 to 2023. His research is on modeling, analysis, optimization, and implementation of emerging communication networks, with an emphasis on wireless networks and time-sensitive traffic. He was a recipient of several research, teaching, and mentoring awards, including the Best Paper Award at IEEE INFOCOM 2018, the Best Paper Award Finalist at ACM MobiHoc 2019, the MIT School of Engineering Graduate Student Extraordinary Teaching and Mentoring Award of 2020, and the 2019–2020 Thomas G. Stockham Jr. Fellowship.

Scientist with Columbia University, from 2020 to 2023. His research is on modeling, analysis, optimization, and implementation of emerging communication networks, with an emphasis on wireless networks and time-sensitive traffic. He was a recipient of several research, teaching, and mentoring awards, including the Best Paper Award at IEEE INFOCOM 2018, the Best Paper Award Finalist at ACM MobiHoc 2019, the MIT School of Engineering Graduate Student Extraordinary Teaching and Mentoring Award of 2020, and the 2019–2020 Thomas G. Stockham Jr. Fellowship.



Carson Garland is currently pursuing the integrated B.S./M.S. degree in electrical engineering with Columbia University. In the past year, he has interned as a Data Engineer with Amazon and is currently conducting video application-focused networking research under Profs. Gil Zussman and Ethan Katz-Bassett. He has interned with both Verizon and AT&T in previous years and holding roles in both radio frequency engineering and data analysis.



Shivan Mukherjee (Student Member, IEEE) is currently pursuing the B.S. degree in computer engineering (minor in operations research) with Columbia University. Previously, he was an Electrical and Firmware Engineering Intern with CLIP Bike. He is also a Student Researcher with the Columbia University Wireless and Mobile Networking Laboratory, focusing on the research of 28 GHz mmWave for fixed wireless access and dense urban deployments.

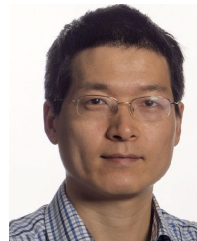


Rodolfo Feick (Life Senior Member, IEEE) received the Ingeniero Civil Electronico degree from Universidad Técnica Federico Santa María (UTFSM), Valparaíso, Chile, in 1970, and the Ph.D. degree in electrical engineering from the University of Pittsburgh, Pittsburgh, PA, USA, in 1975. Since 1975, he has been with the Department of Electronics Engineering, UTFSM, where he is currently an Associate Researcher. His current interests include RF channel modeling, digital communications, microwave system design, and RF measurement.



Dmitry Chizhik (Fellow, IEEE) received the Ph.D. degree in electrophysics from Polytechnic University (now NYU), Brooklyn, NY, USA, in 1991. His Ph.D. thesis was focused on ultrasonics and nondestructive evaluation. He joined the Naval Undersea Warfare Center, New London, CT, USA, where he did research in scattering from ocean floor, geoacoustic modeling of porous media, and shallow water acoustic propagation. In 1996, he joined Nokia Bell Labs, Crawford Hill, Holmdel, NJ, USA, working on radio propagation modeling and measurements,

using deterministic and statistical techniques. He has worked on measurement, modeling, and channel estimation of MIMO channels. The results are used both for the determination of channel-imposed bounds on channel capacity and system performance, and optimal antenna array design. His recent work has included system and link simulations of satellite and femtocell radio communications and millimeter-wave propagation, that included all aspects of the physical layer. His research interests are in acoustic and electromagnetic wave propagation, signal processing, communications, radar, sonar, and medical imaging. He was a recipient of the Bell Labs President's Award.



Jinfeng Du (Member, IEEE) received the B.Eng. degree in electronic information engineering from the University of Science and Technology of China (USTC), Hefei, China, in 2004, and the M.Sc., Tekn. Lic., and Ph.D. degrees from the Royal Institute of Technology (KTH), Stockholm, Sweden, in 2006, 2008, and 2012, respectively. He was a Post-Doctoral Researcher with the Massachusetts Institute of Technology (MIT), Cambridge, MA, USA, from 2013 to 2015, and then he joined the Bell Labs, Crawford Hill, NJ, USA. His research interests are in the general area of wireless communications, especially in communication theory, information theory, wireless networks, millimeter-wave propagation, and channel modeling. He received the Best Paper Award from IC-WCSP in 2010. His paper was elected as one of the best 50 papers at the IEEE GLOBECOM 2014. He received the prestigious Hans Werthen Grant from the Royal Swedish Academy of Engineering Science (IVA) in 2011, the Chinese Government Award for Outstanding Self-Financed Students Abroad in 2012, the International Post-Doc Grant from the Swedish Research Council in 2013, and three grants from the Ericsson Research Foundation.



Reinaldo A. Valenzuela (Life Fellow, IEEE) received the B.Sc. degree from the University of Chile, Santiago, Chile, in 1975, and the Ph.D. degree from Imperial College London, London, U.K., in 1982. He is currently the Director of the Communication Theory Department and a Distinguished Member of Technical Staff with Nokia Bell Labs, Murray Hill, NJ, USA. He has published 190 articles and 44 patents. He has over 33,800 Google Scholar citations. He is engaged in propagation measurements and models, MIMO/space time

systems achieving high capacities using transmit and receive antenna arrays, HetNets, small cells, and next-generation air interface techniques and architectures. He is a member of the National Academy of Engineering, a Bell Labs Fellow, a WWRF Fellow, and a Fulbright Senior Specialist. He was a recipient of the IEEE Eric E. Sumner Award, the 2014 IEEE CTC Technical Achievement Award, and the 2015 IEEE VTS Avant Garde Award. He is a "Highly Cited Author" in Thomson ISI.



Gil Zussman (Fellow, IEEE) received the Ph.D. degree in electrical engineering from Technion in 2004. He was a Post-Doctoral Associate with MIT from 2004 to 2007. He has been with Columbia University since 2007, where he is a Professor of electrical engineering and computer science (affiliated faculty). His research interests are in the area of networking, and in particular in the areas of wireless, mobile, and resilient networks. He received the Fulbright Fellowship, two Marie Curie Fellowships, the DTRA Young Investigator Award, and the NSF CAREER Award. He was a co-recipient of seven paper awards, including the ACM SIGMETRICS'6 Best Paper Award, the 2011 IEEE Communications Society Award for Advances in Communication, and the ACM CoNEXT'6 Best Paper Award. He has been the TPC Chair of IEEE INFOCOM-23, ACM MobiHoc'5, and IFIP Performance 2011. He is the Columbia PI of the NSF PAWR COSMOS testbed.